Chapter 20

ATMOSPHERIC ELECTRICITY

Section 20.1 R.C. Sagalyn and H.K. Burke
Section 20.2 D.R. Fitzgerald

20.1 FAIR WEATHER ELECTRICITY

Electric fields, currents, and conductivities as well as positive and negative ions of greatly varying size and composition constitute the principal electrical properties of the atmosphere in fair weather. Air mass motions, pressure systems, winds, turbulence, temperature, and water vapor distributions have an important influence on the electrical properties in the troposphere through their control over the distributions of charged and uncharged aerosols and radioactive particles of terrestrial origin. These influences are greatest in the atmospheric exchange layer which is generally restricted to 2.5 km above the earth's surface. In the altitude region 30 to 90 km there is a transition from classical concepts of atmospheric electricity to the phenomena of ionospheric physics chiefly because of the changing atmospheric composition and increasing mean free path resulting in an increase in the concentration of free electrons. Recent studies have shown that the ionosphere, with its relatively high conductivity, can no longer be regarded as the upper bound for atmospheric electrical processes. The exact nature of electrical coupling to the ionospheric and magnetospheric regions is currently under investigation.

20.1.1 Electrical Conductivity

The lower atmosphere is a slightly conducting medium due to the presence of positive and negative ions. The principal sources of ionization include (1) cosmic radiation, (2) radiation from radioactive substances in soil, and (3) radioactive gases produced by the decay of (2). Among them (1) is mainly responsible for air conductivity at higher altitudes while (2) and (3) are dominant in the lower atmosphere. Table 20-1 shows average ion pair production rates due to radioactivity and cosmic radiation between 0 and 10 km.

The conductivity σ of air is defined as

$$\sigma = \sum_{i=1}^{m} n_i e_i k_i , \qquad (20.1)$$

where m is the number of different ion species present, and n_i, e_i, and k_i are the number density, charge, and mobility of the i^{th} ion species respectively. Small ions because of their low mass have higher mobility than large ions. Over 95% of the total conductivity of the air is contributed by small ions so that

$$\sigma \approx n_+ ek_+ + n_- ek_- \qquad (20.2)$$

where n_+ and n_- are number densities of positive and negative small ions and k_+ and k_- are their mobilities. The mobility of an ion is its velocity per unit electric field strength. Near the earth's surface, $n_+ \approx 600$ cm^{-3}, $n_- \approx 500$ cm^{-3}, $k_+ \approx 1.3$ cm^{2}V^{-1}s^{-1} and $k^- \approx 1.6$ cm^{2}V^{-1}s^{-1} yielding a conductivity of about 2.5×10^{-14} ohm^{-1}m^{-1}.

The conductivity of air increases rapidly with altitude for the following reasons: (1) the mobility of ions increases as the neutral number density decreases (Figure 20-1), (2) the presence of numerous large aerosols lowers the conductivity of air near the ground and (3) the cosmic radiation causes an increase in the concentration of small ions with altitude (Table 20-1).

To a first approximation, ion equilibrium exists above the exchange layer (that is, above 2.5 km) so that $q = \alpha n_{\pm}^2$, where q is the net production rate of small ions and α is the volume recombination coefficient. If $k_+ \cong k_-$

Table 20-1. Average ion-pair production rates due to radioactivity and cosmic radiation as a function of altitude [Sagalyn and Fitzgerald, 1965].

Altitude (km)	Ion pairs (cm^{-3}s^{-1}) radioactive	cosmic rays	Total
0	7.6	1.5	9.1
0.5	3.8	1.8	5.6
1	2.7	2.6	5.3
2	1.5	5.0	6.5
3	0.9	8.0	8.9
4	0.5	15.0	15.5
5	0.3	23.0	23.3
6	—	37.0	37.0
8	—	75.0	75.0
10	—	125.0	125.0

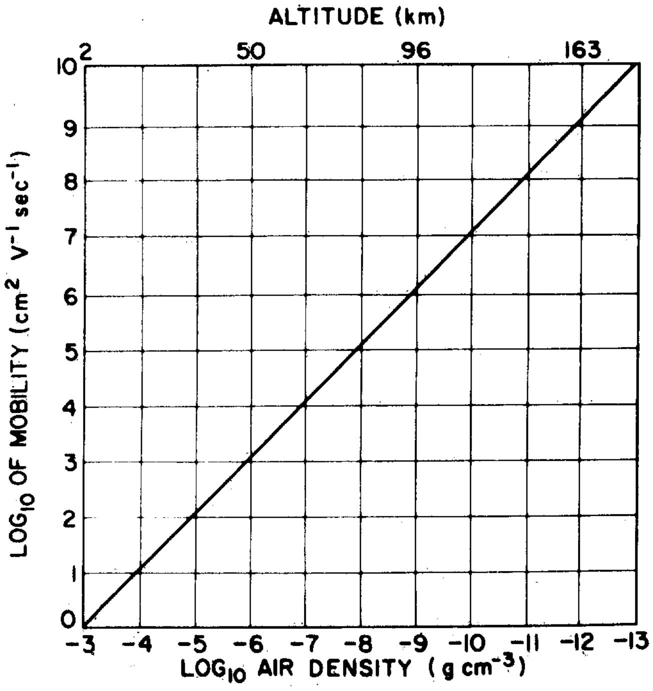

Figure 20-1. Mobility of small positive or negative ions vs air density or altitude, assuming k = 1.4 cm²V⁻¹s⁻¹ at 273 K and 1013.25 mb pressure.

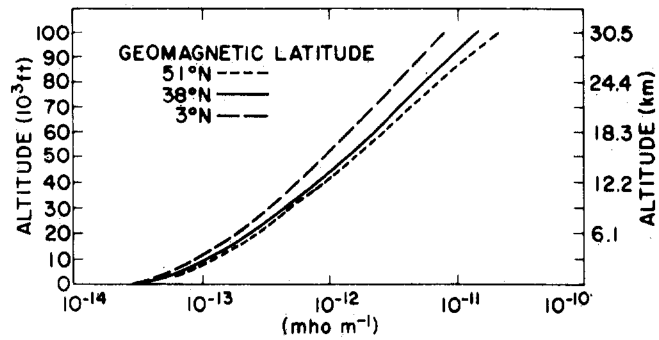

Figure 20-3. Total electrical volume conductivity vs altitude.

= k is also assumed, the electrical conductivity can then be given by

$$\sigma = 2ek\sqrt{q/\alpha}\ . \qquad (20.3)$$

Figure 20-2 shows the variation of α with altitude. Figure 20-3 shows the computed variation of volume conductivity with altitude. Values of q are derived from cosmic ray ionization rates; values of k and α are taken from Figures 20-1 and 20-2, respectively.

Variations of electrical conductivity in the atmosphere as a function of altitude have been measured by a number of workers. See Figure 20-4. In this figure, curves 2 through 5 represent earlier experimental results. Curve 1 was calculated by Cole and Pierce [1965] based on variations of electron and ion concentrations and effective collisional frequencies with respect to altitude. The curve 1 values are higher than the others probably because Cole and Pierce neglected large ions. Curve 2 was compiled by Sagalyn [1965] from experimental results prior to 1963. Curves 3, 4, and 5 were obtained from measurements of Paltridge [1965], Mozer and Serlin [1969], and Morita et al. [1971], respectively. Curves 6, 7, and 8 show more recent measurement over Laramie, Wyoming; Hilo, Hawaii; and Sanriku, Japan, respectively. The Laramie measurements were obtained as part of an international effort on Atmospheric Electrical Measurements in 1978 [Rosen et al., 1980]. The 1978 measurements over Laramie are similar to results obtained at the same location in 1974 and 1975 [Takagi et al., 1980]. Positive and negative ion density measurements were combined and smoothed to provide the total conductivity (curve 6). Takagi et al. [1980] also published conductivity profiles for Sanriku, Japan (1973–1975) and Hilo, Hawaii (1975) (curves 7 and 8).

The differences in the conductivity profiles of Figure 20-4 are largely due to the latitude of measurement, envi-

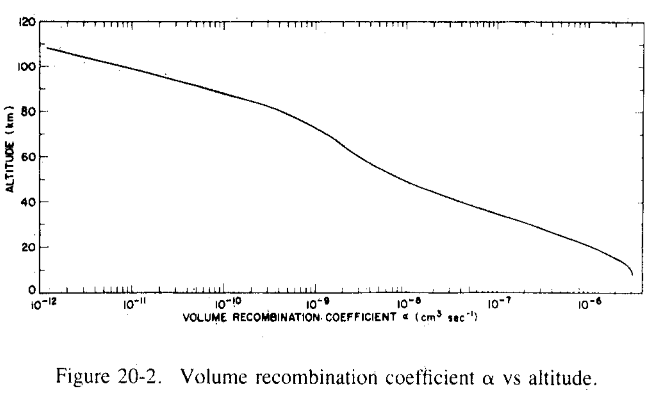

Figure 20-2. Volume recombination coefficient α vs altitude.

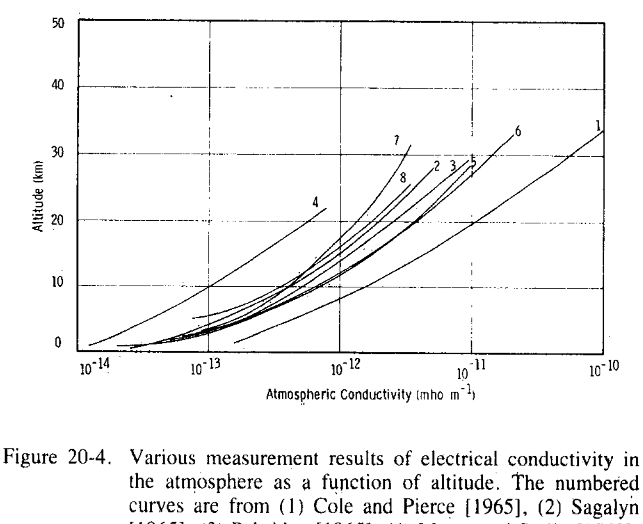

Figure 20-4. Various measurement results of electrical conductivity in the atmosphere as a function of altitude. The numbered curves are from (1) Cole and Pierce [1965], (2) Sagalyn [1965], (3) Paltridge [1965], (4) Mozer and Serlin [1969], (5) Morita et al. [1971], (6) Rosen et al. [1980] for Laramie, Wyoming, (7) Takagi et al. [1980] for Sanriku, Japan, and (8) Takagi et al. [1980] for Hilo, Hawaii.

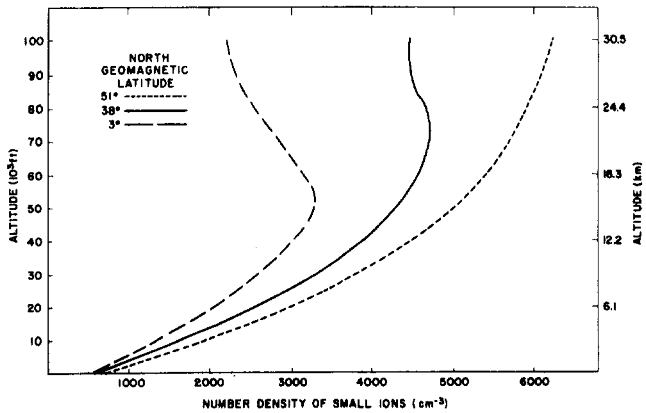

Figure 20-5. Number density of small positive or negative ions vs altitude computed from $q = \alpha\, n_{\pm}^2$. The variation with latitude illustrates the effect of cosmic rays on production rates.

ronmental conditions at the time of measurement, and the data base upon which the curves were derived. For example, curve 2 [Sagalyn, 1965] is based on the results of approximately 100 aircraft and balloon flights. A large percentage of the flights were conducted in the industrial northeastern part of the U.S. where significant aerosol concentrations exist throughout the troposphere.

The differences in the more recent measurements (curves 6 to 8) can probably be attributed to the latitude variation of cosmic ray intensities which in turn affect the small ion concentration. See, for example, Figure 20-5. Because the conductivity is roughly proportional to the square root of the small ion concentration (Equation (20.3)), the conductivity at Laramie (50° geomagnetic) is expected to be approximately twice as large as that at Sanriku (29° geomagnetic) and Hilo (20° geomagnetic). Figure 20-6 shows the variation with latitude of the average (base) electrical conductivity, the latitude variation following a solar flare, and that expected as a result of Forbush decrease [Hays and Roble, 1979].

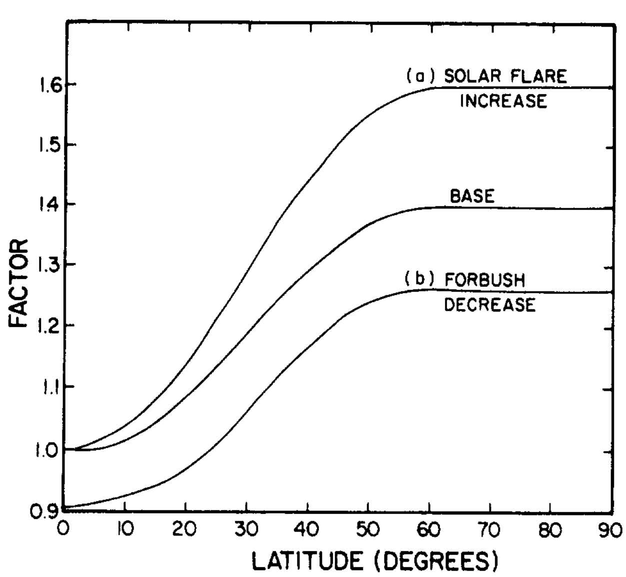

Figure 20-6. Relative variation of electrical conductivity σ/α_u with latitude for different environmental conditions: (a) solar flare, (b) Forbush Decrease [Hays and Roble, 1979].

The conductivity variation with altitude is approximated by the relation

$$\sigma(z) = \sigma_0 \exp(2kz), \tag{20.4}$$

where $(2\,k)^{-1}$ is defined as the scale height of conductivity. It varies typically between 5 and 6 km. The conductivity at the surface, σ_0, varies between 1 and 3 $\times$ 10^{-14} ohm^{-1} m^{-1}.

20.1.2 Electric Field

In fair weather areas the horizontal components of the field are small compared to the vertical component so that the atmospheric electric field E can be defined as

$$E = -\frac{dV}{dZ}, \tag{20.5}$$

where V is the electric potential and Z is the altitude. The atmospheric electric field is directed vertically, the potential gradient decreases with increasing altitude, and the field by the electrostatic definition is negative (field vector directed downward). Computed from the current density and mobility, Figure 20-7a shows the expected electric field as a function of altitude. Figure 20-7b shows the average value and variation of a measured electric field as a function of altitude [Sagalyn, 1965].

Large scale mappings of the atmospheric electric field which took into account the variational property of air conductivity were carried out by Holzer and Saxon [1952] and Anderson and Freier [1969]. These models do not extend into the ionosphere where the conductivity has a tensor

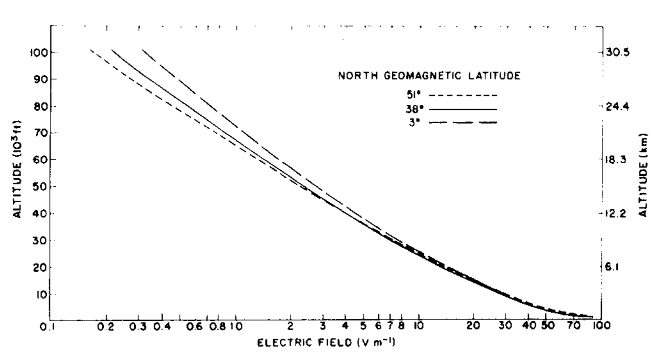

Figure 20-7a. Electric field vs altitude, assuming a conduction current density of 2.7×10^{-12} A m^{-1} and using values of α from Figure 20-2.

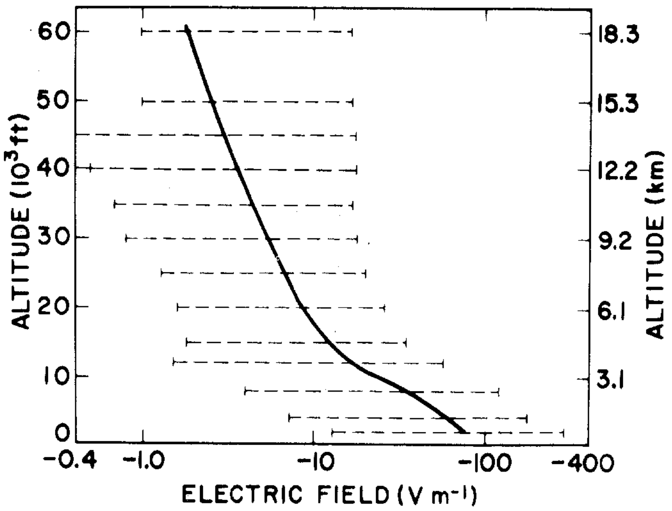

Figure 20-7b. Average value and maximum variation of electric field as a function of altitude in over 80 aircraft and balloon flights in the eastern U.S. [Sagalyn, 1965].

rather than a scalar form. Park and Dejnakarintra [1973] mapped thundercloud electric fields at middle and higher latitudes. The electrical conductivity was represented as an exponential function of altitude, and the anisotropy of air was taken into account above 70 km. The high-latitude magnetic field lines were assumed to be vertical below 150 km and numerical solutions were derived for both the atmosphere and ionosphere.

Assuming an exponential increase in conductivity with altitude, the basic equations for the atmospheric electric field can be expressed:

$$\sigma(z) = \sigma_0 \exp(2kz) \qquad (20.4)$$

$$\nabla \times \mathbf{E} = 0, \text{ or } \mathbf{E} = -\nabla\Phi \qquad (20.6)$$

where Φ is the electric potential with respect to the earth's surface.

The potential equation is

$$\left[\nabla^2 + 2k\frac{\partial}{\partial z}\right]\Phi = -f/\varepsilon_0, \qquad (20.7)$$

where f is the known source distribution (ρ_{source}). In fair weather there is no charge source and the potential equation reduces to

$$\left[\nabla^2 + 2k\frac{\partial}{\partial z}\right]\Phi = 0. \qquad (20.8)$$

Applying appropriate boundary conditions, the fair weather electric field components can be expressed as follows:

$$E_x = 0,$$

$$E_y = 0, \text{ and} \qquad (20.9)$$

$$E_z = -\frac{V_0 \cdot 2k}{1 - e^{-2kH}},$$

where V_0 is the total potential difference between the top of the atmosphere and the earth's surface and H is the upper boundary of the atmosphere. In the solution for the fair weather electric field, only the vertical component exists.

Defining $E_0 \equiv -[V_0 \cdot 2k/(1 - e^{-2kH})]$ as the field intensity near the ground, the fair weather electric field can be rewritten as

$$E_z = E_0\, e^{-2kz}. \qquad (20.10)$$

The average observed values of E_0 over land is about 130 V/m in fair weather. Based on this value, the electric field at the 70 km level is 0.1 mV/m to 1 mV/m. This is the same order of magnitude of electric fields of magnetospheric origin. During disturbed weather conditions, much larger fields have been observed.

20.1.3 Currents and Space Charge

20.1.3.1 Air-Earth Conduction Current. As a result of the existence of predominately vertical electric field in the presence of positive and negative atmospheric ions, a current is constantly flowing to the earth's surface. This current is called the air-earth conduction current. The vertical conduction current density j is defined by

$$j = V/R_c = \sigma\, E. \qquad (20.11)$$

The potential difference between the earth and the upper atmosphere conducting layers V is $-\int_0^\infty E\, dZ$. The resistance of a vertical air column per unit area R_c is $\int_0^\infty dZ/\sigma$. Conservation of charge and continuity considerations requires that the current along the column be nearly constant. The conduction current density is, therefore, the net vertical current due to positive ions flowing downward and negative ions flowing upward in the atmosphere. Measurements show that despite large variations in the electric field and atmospheric conductivity, the air-earth conduction current is comparatively stable (Table 20-2). The mean value of air-earth current density from annual observations is 2.3 pA (picoamps)/m^2 over continents and 3.3 pA/m^2 over oceans [Israël and Dolezalek 1973]. The zonal distribution given in Table 20-2 was derived by Hogg [1950].

The mean diurnal variation of the air-earth current density for 10 continental stations derived from data obtained over at least one year is given in Figure 20-8. The diurnal

Table 20-2. Zonal distributions of air-earth current densities.

Latitude Zone	Mean Current Density (pA/m^2)
Arctic	3.0
Northern temperate zone	2.1
Tropics	2.6
Southern temperate zone	2.4
Antarctic	3.0

variations are given in percentages to facilitate comparisons [Israël and Dolezalek, 1973]. The early morning increase in current density is attributed to the "sunrise effect" also observed by Burke and Few [1978]. Local effects such as visibility, fog, and humidity can also reduce the current density. Figure 20-9 shows some recent direct measurements of air-earth current density at different altitudes and locations. There are other atmospheric currents such as the convection current that should be distinguished from the conduction current.

20.1.3.2 Convection Current. In regions where a space charge exists (excess of ions of one sign), movement of air produces a transfer of charge that can be defined as a convection current density j_2

$$j_2 = \rho v \approx A_\sigma \frac{\partial \rho}{\partial Z}, \qquad (20.12)$$

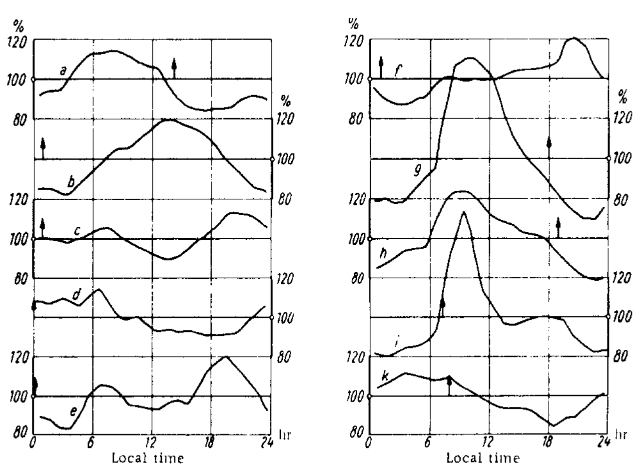

Figure 20-8. Mean diurnal variation of the air-earth current density (according to data over at least one year) at 10 stations in percentage representation. The stations have been arranged according to geographic latitude. The arrows on the time axis represent 0 h GMT: (a) Fairbanks, Alaska; (b) Uppsala, Sweden; (c) Potsdam, E. Germany; (d) Kew, England; (e) Chambon-la-Foret, France; (f) Buchau, Germany; (g) Tucson, Arizona; (h) Huancayo, Peru; (i) Bandung, Indonesia; and (k) Watheroo, W. Australia [Israël and Dolezalek, 1973].

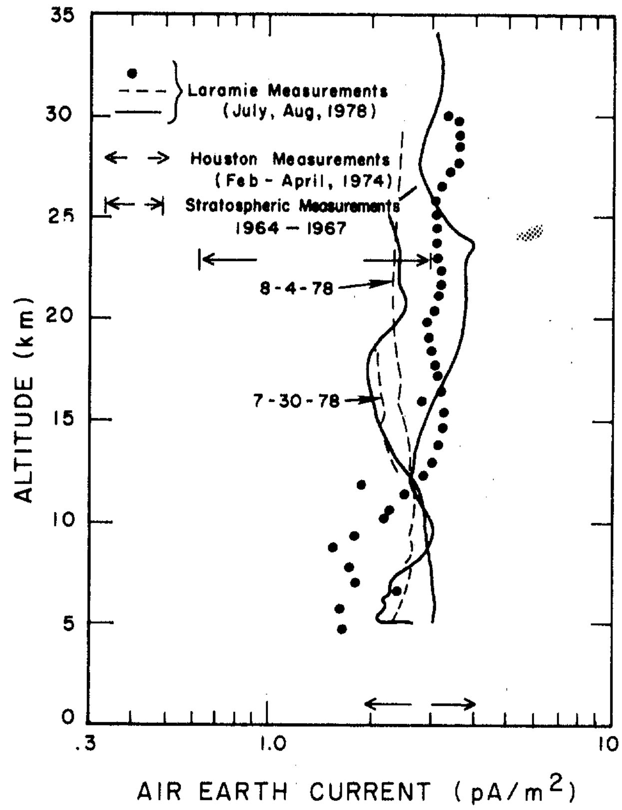

Figure 20-9. Direct measurements of the air-earth-current as reported by several different groups:
1978 Laramie Measurements [Rosen et al., 1980]
1974 Houston Measurements [Burke and Few, 1978]
1964–67 Stratospheric Measurements [Uchikawa, 1972]

where ρ is the space charge per unit volume, v is the vertical air velocity, and A_σ is the coefficient of eddy diffusion. Space charge densities and gradients large enough to significantly influence the vertical current occur primarily in the exchange (Austausch) layer, where considerable mixing occurs and greatly varying quantities of charged nuclei are introduced into the atmosphere. Throughout this chapter, nuclei refer to molecular aggregates that may or may not act as condensation nuclei depending on their chemical composition.

Aspinall [1972] showed that the conduction current and mechanical transfer currents, which include the convection current, are about the same order of magnitude in the exchange layer. Convection currents comparable to or greater than the conduction current have been observed below 0.015 km [Smith, 1958].

The space charge density ρ is related to the field and to the potential through Poisson's equation

$$\frac{dE}{dZ} = \frac{d^2V}{dZ^2} = -4\pi\rho \qquad (20.13)$$

in cgs electrostatic units.

20.1.3.3 Displacement Current. A displacement current exists when the electric field (potential gradient) changes with time.

$$j_{displacement} = \varepsilon_o \frac{dE}{dt}$$

Thus, when there exists a significant variation of the electric field with time, instantaneous measurements of the air-earth current will be made up of the sum of the displacement current and the conduction current.

20.1.3.4 "Electrode Effect." As a result of the earth's negative charge, negative ions drift upward near the surface of the earth and unless they are replaced by negative ions from radioactive substances in the ground they will leave a region of net positive charge near the surface. This phenomena is referred to as the "electrode effect." Hoppel [1969], comparing theories of the atmospheric electrode effect with the experimental observations of Crozier [1965], Gathman [1967], and Muhleisen [1961] concluded that within the first quarter of a meter above ground there is a region of positive space charge. Above that height, positive ions are balanced by an upward flow of negative ions from radioactive sources. The reverse of the normal electrode effect is sometimes observed on quiet nights due to the trapping of these radioactive ions. Over water or over the polar caps the electrode effect is observed to extend to higher altitudes due to the absence of ions from radioactive sources.

20.1.3.5 Earth Charge and Worldwide Current System. The total conduction current flowing to the earth at any given time is approximately 1800 amperes. As a result of this current, the bound negative charge of the earth (about 500 000 C) would be neutralized in less than half an hour. The net charge, however, remains nearly constant. Thunderstorms and lightning shower clouds are the most likely mechanisms for the maintenance of the earth's charge. Stergis [1957] found that thunderstorm and shower clouds act as generators, driving current upward in the reverse direction to the current flow in fair weather areas. Lightning discharges are also found to carry negative charges to earth in large amounts for short periods of time. It is estimated that a large portion of the 1800 ampere global conduction current is balanced by the charge of opposite sign transferred by the lightning activity of thunderstorms throughout the world.

It should be noted that the potential gradient in undisturbed fair weather areas has the same diurnal variation over all the earth when referred to universal time [Mauchly, 1923]. This diurnal variation is in phase with the diurnal variation of worldwide thunderstorm activity. The potential gradient in undisturbed areas is proportional to the total potential difference between the earth and ionosphere. The magnitude of this potential difference is 275 ± 50 kV.

20.1.4 Atmospheric Ions

20.1.4.1 Definition and Relations. Atmospheric ions are divided into four main groups according to their size and mobilities: small positive and negative ions, n_+ and n_-, and large positive and negative ions (also referred to as charged nuclei), N_1 and N_2. Table 20-3 gives the range of mobilities and radii of atmospheric ions.

The continuity equations for the production and destruction of ions may be written

$$\frac{dn_+}{dt} = q_1 - \alpha n_+ n_- - \eta_{12} n_+ n_- - \eta_{10} n_+ N_o, \quad (20.14)$$

$$\frac{dn_-}{dt} = q_2 - \alpha n_+ n_- - \eta_{21} n_- N_1 - \eta_{20} n_- N_o, \quad (20.15)$$

$$\frac{dN_1}{dt} = Q_1 - \eta_{10} n_+ N_o - \eta_{21} n_- N_1 - \gamma N_1 N_2, \quad (20.16)$$

$$\frac{dN_2}{dt} = Q_2 - \eta n_- N_o - \eta_{12} n_+ N_2 - \gamma N_1 N_2, \quad (20.17)$$

where q_1 and q_2 are net production rates of small ions due to radioactive emanations from the earth's surface, cosmic radiation and diffusion, and Q_1 and Q_2 are net production rates of large ions due to ionizing sources and diffusion ($q_1 \approx q_2$ and $Q_1 \approx Q_2$). N_o is the concentration of neutral nuclei. The volume recombination coefficient for small ions is, in $cm^{-3}s^{-1}$,

$$\alpha = 1.75 \times 10^{-5} \left(\frac{273}{T}\right)^{2/3} (2M)^{-1/2} f(Y), \quad (20.18)$$

Table 20-3. Mobility and size range of atmospheric ions.

Ions	Mobility ($cm^2s^{-1}V^{-1}$)	Radius (cm)
Small	1 to 2	6.6×10^{-8} to 7.8×10^{-7}
Average large	10^{-3} to 10^{-2}	7.8×10^{-7} to 2.5×10^{-6}
Langevin	2.5×10^{-4} to 10^{-3}	2.5×10^{-6} to 5.7×10^{-6}
Ultra large	$< 2.5 \times 10^{-4}$	$> 5.7 \times 10^{-6}$

where T is the temperature in K, M is the molecular weight of the ions in atomic mass units, and f(Y) is the probability function.

$$f(Y) = 1 - 4Y^{-4}\left[1 - (Y + 1)\,e^{-Y}\right]^2, \quad (20.19)$$

and

$$Y = 0.81\left(\frac{273}{T}\right)^2\left(\frac{P}{760}\right)\left(\frac{L_A}{L}\right). \quad (20.20)$$

P is the pressure in mm H_g and L_A/L is the ratio of the mean free path of a molecule to that of an ion at normal temperature and pressure; for air, $L_A/L = 3$. Table 20-4 gives values of f(Y) for Y between 0 and 2.5. The variation of α with altitude was shown previously in Figure 20-2.

The attachment coefficients are η_{12} for collisions between small positive and large negative ions, η_{21} for collisions between small negative and large positive ions, η_{10} for collisions between small positive ion and a neutral nucleus, and η_{20} for collisions between a small negative ion and a neutral nucleus. Bricard [1949] derived expressions for these attachment coefficients as a function of the charge and radius of the nuclei and mobility and diffusion coefficient of the small ion. The diffusion coefficients of small positive and negative ions are approximately equal, therefore

$$\eta_{12} \approx \eta_{21} = 4\,\pi D\, a/I\,(\zeta, p), \quad (20.21)$$

$$\eta_{20} \approx \eta_{10} = 4\,\pi D\, a/I\,(\zeta, o), \quad (20.22)$$

where D is the average value of the small diffusion coefficient, a is the radius of the interacting charged or uncharged nucleus, and I (ζ, p) is a dimensionless parameter that contains the dependence of the attachment coefficient on the radius and charge of the nucleus.

$$I\,(\zeta, p) = \int_1^{\infty} X^{-2} \exp\left[-\zeta\left(\frac{p}{X} + \frac{1}{2\,X^2\,(X^2 - 1)}\right)\right] dX \quad (20.23)$$

where p is the number of elementary charges on the large ion, $\zeta = ek/Da$ in cgs electrostatic units, or $\zeta = ek/4\,\pi\,\varepsilon_o\,Da$ in mks units (k is small-ion mobility), and $X = r/a$, where r is the radius of a sphere of influence centered on the nucleus. Figure 20-10 gives values of I (ζ, p).

In Equations (20.16) and (20.17), γ is the combination

Table 20-4. Probability function f (Y) from Equation (20.20).

Y	0	1	2	3	4	5	6	7	8	9
0.03	0.03916	0.04044	0.04172	0.04299	0.04426	0.04553	0.04680	0.04806	0.04933	0.05059
0.04	0.05185	0.05311	0.05437	0.05562	0.05688	0.05813	0.05938	0.06063	0.06187	0.06312
0.05	0.06436	0.06560	0.06684	0.6808	0.06932	0.07055	0.07179	0.07302	0.07425	0.07547
0.06	0.07670	0.07792	0.07914	0.08037	0.08158	0.08280	0.08402	0.08523	0.08644	0.08765
0.07	0.08886	0.09007	0.09127	0.09248	0.09368	0.09488	0.09608	0.09727	0.09847	0.09966
0.08	0.1009	0.1020	0.1032	0.1044	0.1056	0.1068	0.1080	0.1091	0.1103	0.1115
0.09	0.1127	0.1138	0.1150	0.1162	0.1174	0.1185	0.1197	0.1209	0.1220	0.1232
0.1	0.1243	0.1358	0.1472	0.1583	0.1694	0.1802	0.1910	0.2015	0.2119	0.2222
0.2	0.2324	0.2423	0.2522	0.2619	0.2715	0.2809	0.2903	0.2994	0.3085	0.3175
0.3	0.3263	0.3350	0.3435	0.3520	0.3603	0.3686	0.3767	0.3847	0.3926	0.4004
0.4	0.4080	0.4156	0.4231	0.4304	0.4377	0.4449	0.4519	0.4589	0.4658	0.4726
0.5	0.4793	0.4859	0.4924	0.4988	0.5051	0.5114	0.5175	0.5236	0.5296	0.5355
0.6	0.5414	0.5471	0.5528	0.5584	0.5639	0.5694	0.5748	0.5801	0.5853	0.5905
0.7	0.5956	0.6006	0.6056	0.6105	0.6153	0.6201	0.6248	0.6294	0.6340	0.6385
0.8	0.6430	0.6474	0.6517	0.6560	0.6602	0.6644	0.6685	0.6726	0.6766	0.6805
0.9	0.6844	0.6883	0.6921	0.6958	0.6995	0.7032	0.7068	0.7103	0.7138	0.7173
1.0	0.7207	0.7241	0.7274	0.7307	0.7339	0.7371	0.7403	0.7434	0.7465	0.7495
1.1	0.7525	0.7555	0.7584	0.7613	0.7641	0.7669	0.7697	0.7724	0.7751	0.7778
1.2	0.7804	0.7830	0.7856	0.7881	0.7906	0.7931	0.7955	0.7979	0.8003	0.8027
1.3	0.8050	0.8072	0.8095	0.8117	0.8139	0.8161	0.8182	0.8203	0.8224	0.8245
1.4	0.8265	0.8285	0.8305	0.8325	0.8344	0.8363	0.8382	0.8401	0.8419	0.8437
1.5	0.8455	0.8473	0.8490	0.8508	0.8525	0.8541	0.8558	0.8574	0.8591	0.8607
1.6	0.8623	0.8638	0.8654	0.8669	0.8684	0.8699	0.8713	0.8728	0.8742	0.8756
1.7	0.8770	0.8784	0.8796	0.8811	0.8824	0.8837	0.8850	0.8863	0.8876	0.8888
1.8	0.8901	0.8913	0.8925	0.8937	0.8948	0.8960	0.8971	0.8983	0.8994	0.9005
1.9	0.9016	0.9027	0.9037	0.9048	0.9058	0.9068	0.9079	0.9089	0.9098	0.9108
2.0	0.9118	0.9127	0.9137	0.9146	9.9154	0.9165	0.9174	0.9182	0.9191	0.9200
2.1	0.9208	0.9217	0.9225	0.9233	0.9242	0.9250	0.9258	0.9266	0.9273	0.9281
2.2	0.9289	0.9296	0.9304	0.9311	0.9318	0.9325	0.9332	0.9339	0.9346	0.9353
2.3	0.9360	0.9367	0.9373	0.9380	0.9386	0.9393	0.9399	0.9405	0.9411	0.9417
2.4	0.9423	0.9429	0.9435	0.9441	0.9447	0.9452	0.9458	0.9464	0.9469	0.9475

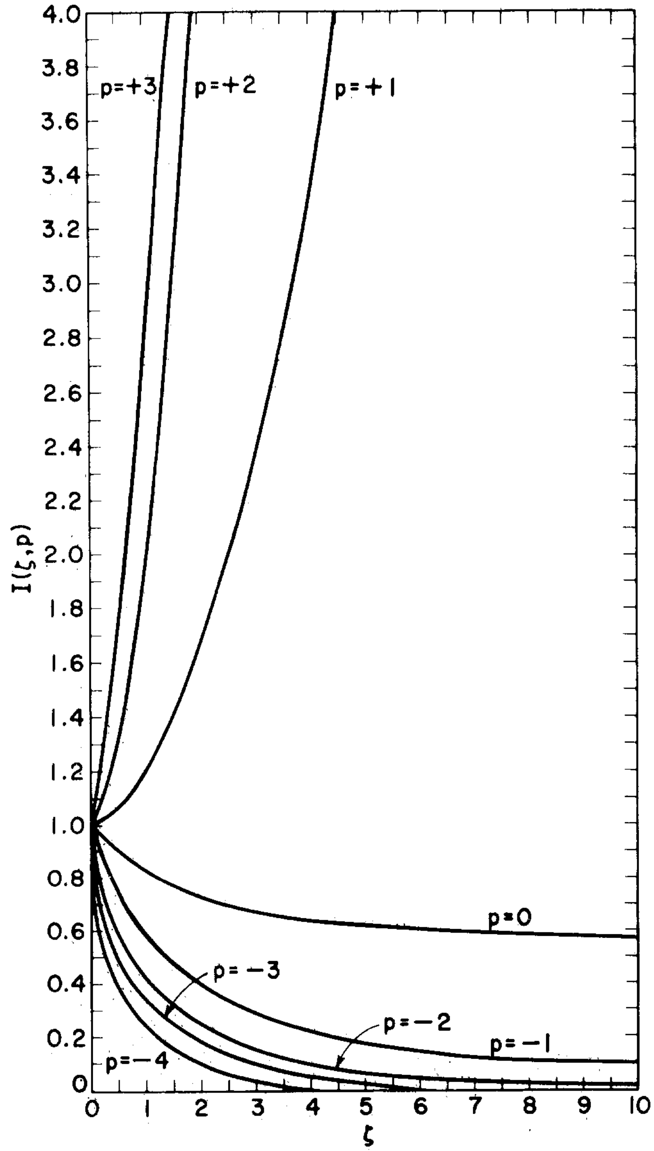

Figure 20-10. Parameter I (ζ,p) for Equations (20.21) and (20.22); p is the number of positive or negative elementary charges on the large ion; and ζ is a dimensionless parameter.

coefficient for collisions between large ions of opposite sign with a value of approximately 10^{-9} cm^3s^{-1}. This is three orders of magnitude less than the value of the attachment coefficients so that terms containing γ, therefore, can usually be neglected.

20.1.4.2 Positive Ion Chemistry and Composition in the Stratosphere and Troposphere. A positive ion reaction scheme for the stratosphere and troposphere is given in Figure 20-11a and b [Ferguson, 1979]. It is essentially the O_2^+ reaction sequence of the D-region positive ion chemistry augmented by reactions that involve some of the minor constituents of the lower atmosphere. See also Chapter 21.

Variations of typical ionization production rates in the troposphere are shown in Figure 20-12. Values of less than

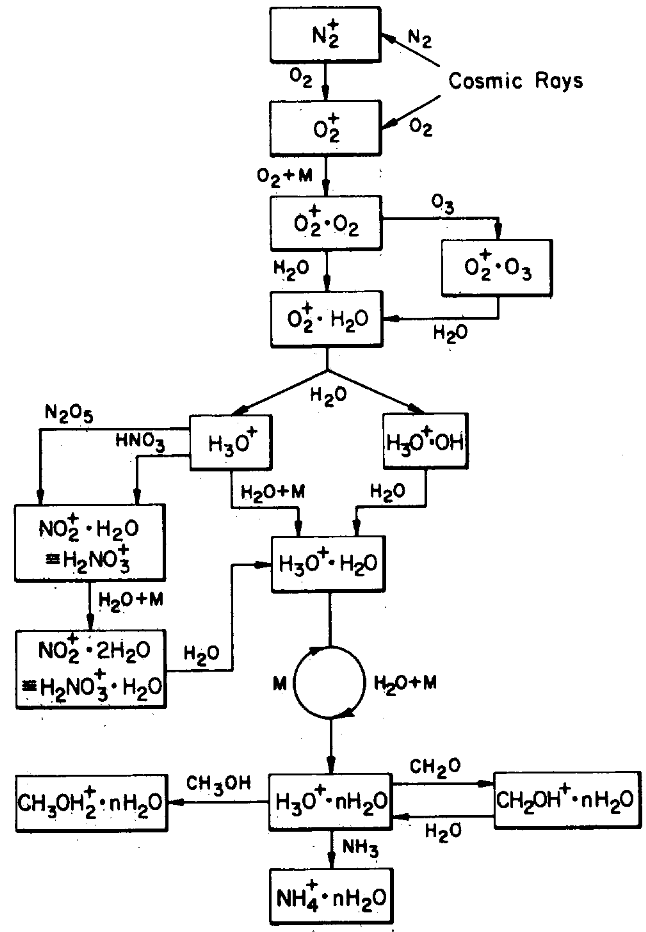

Figure 20-11a. Stratospheric positive ion chemistry [Ferguson et al., 1979].

1 to more than 20 ion pairs $cm^{-3}s^{-1}$ occur in the stratosphere. The ambient concentration of positive ions is determined by the recombination rate with negative ions. The ion concentration in the lower stratosphere has been found to have a value of about 5×10^3 cm^{-3}. Positive ion lifetimes are on the order of a few thousand seconds.

As shown in Figure 20-11a and b, the initial products of the ionization below 60 km are predominantly N_2^+ and O_2^+, with lesser amounts of O^+ and N^+. These ions are rapidly converted to O_2^+, as well as an inconsequential amount of NO^+, by well-established reactions. Once formed, the O_2^+ ions associate with O_2

$$O_2^+ + O_2 + M \rightleftarrows O_2 \cdot O_2^+ + M. \quad (20.24)$$

The formation of $O_2^+ \cdot O_2$ begins a series of fast switching reactions (see Figure 20-11b) that involve H_2O and leads to the formation of the water cluster ions, $H_3O^+ \cdot nH_2O$.

In the troposphere, where the H_2O mixing ratio is about 10^{-2}, the conversion of $O_2^+ \cdot O_2$ to $O_2^+ \cdot H_2O$ proceeds so rapidly that the reacting rates outlined must lead to the water cluster ions. However, in the stratosphere, where the H_2O mixing ratio is of the order of 10^{-6}, other neutral con-

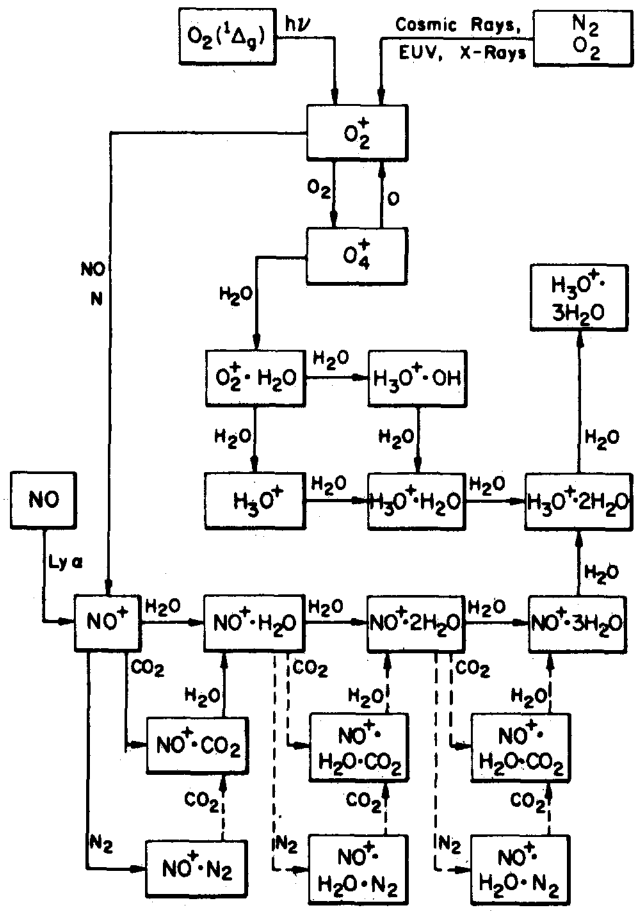

Figure 20-11b. D-region positive ion chemistry [Ferguson et al., 1979].

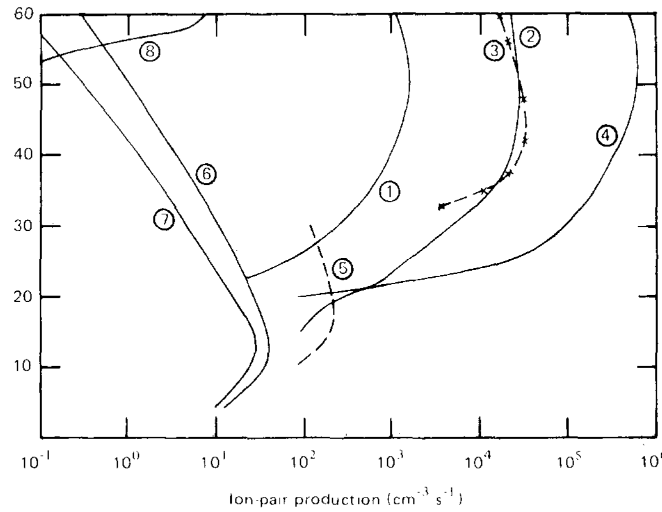

Figure 20-12. Ion-pair production rates due to solar protons: (1) Polar cap absorption (PCA), 11/2/69; (2) PCA, 8/4/72; 1500–1600 UT; (3) PCA, 8/4/72, 1508 UT; (4) PCA, 8/4/72, 2200 UT; (5) PCA 9/29/61; (6) SSMIN (sunspot minimum) galactic cosmic rays; (7) SSMAX (sunspot maximum) galactic cosmic rays; and (8) precipitating electrons in a hard aurora [Herman and Goldberg, 1978a].

stituents have comparable abundances. CO_2 has a much larger concentration and O_3 and CH_4 concentrations are comparable with that of H_2O. If $O_2^+ \cdot O_2$ reacts with any of these neutrals, then the ion chemistry outlined in Figure 20-11 might be significantly altered.

These $O_2^+ \cdot O_2$ reactions have been examined and the results are given in Table 20-5. The first entry is the fast reaction against which the alternative paths must compete. In contrast, the reaction of $O_2^+ \cdot O_2$ with CH_4 is very slow. The reactions of $O_2^+ \cdot O_2$ with CO_2 and O_3 were studied in equilibrium and the thermochemical constants are given. However, the exothermicity for the reaction involving O_3 is much larger; therefore, the $O_2^+ \cdot CO_2$ and $O_2^+ \cdot O_3$ ion concentrations will be more comparable. The $O_2^+ \cdot O_3$ concentrations are estimated to never drop below one tenth of the $O_2^+ \cdot O_2$ concentration and even equal it at 30 km. This means that the $O_2^+ \cdot O_3$ chemistry must also be considered.

Recently, the first stratospheric ion composition measurements were made in rocket-borne mass-spectrometer flights. Three high-latitude studies sampled the positive ions during descent through the altitude range 55 to 35 km.

Above 45 km, the substantial signal levels permitted high resolution identification of the water cluster ions $H_3O^+ \cdot nH_2O$ with n = 9, 1, 2, and 3 as the dominant species in this region. A rather sharp transition at about 45 km was reported from the water cluster ions to ions with e/m ratios of 29 ± 2, 42 ± 2, 60 ± 2, and 80 ± 2. In the region below this altitude, the cluster ions that do not

Table 20-5. $O_2^+ \cdot O_2$ reactions with H_2O, Ch_4, CO_2, and O_3 (300 K).

Reactions	Result[a]	Source
1. $O_2^+ \cdot O_2 + H_2O \rightarrow O_2^+ \cdot H_2O + O_2$	$k = 1.5(-9)\ cm^3\ s^{-1}$	Howard et al. (1972)
2. $O_2^+ \cdot O_2 + CH_4 \rightarrow$ products	$k < 3(-12)\ cm^3\ s^{-1}$	Dotan et al. (1978)
3. $O_2^+ \cdot O_2 + CO_2 \rightleftarrows O_2^+ \cdot CO_2 + O_2$	$\Delta H = 0.3 \pm 1.0$ kcal $mole^{-1}$ $\Delta S = 4.3 \pm 2.6$ cal $mole^{-1} K^{-1}$	Dotan et al. (1978)
4. $O_2^+ \cdot O_2 + O_3 \rightleftarrows O_2 \cdot O_2^+ \cdot O_3 + O_2$	$\Delta H = -3.7 \pm 1.0$ kcal $mole^{-1}$ $\Delta S = 4.5 \pm 2.6$ cal $mole^{-1} K^{-1}$	Dotan et al. (1978)

[a] 1.5(−9) implies 1.5×10^{-9}.

contain H_2O become the dominant species. More recent balloon flights indicate that water cluster ions are the major species at 35 km. Other ions were observed in appreciable concentration, in particular ions with an e/m ratio of 96 ± 2.

The observation of water cluster ions as the dominant species down to altitudes of 45 km or below, have been formed undoubtedly by the chemistry described in Figure 20-11a. Those observations place upper limits on the neutral molecules that react rapidly with $H_3O^+ \cdot nH_2O$ ions.

There is a clear need for more detailed measurements of stratospheric and tropospheric positive ions with instruments of higher mass resolution. There is also a need for measurements of the critical neutral constituents for the ion chemistry, such as NaOH.

20.1.4.3 Negative Ion Chemistry and Composition in the Stratosphere and Troposphere. The negative ion chemistry of the stratosphere and troposphere is even more speculative than the positive ion chemistry of these regions. In addition to there being few measurements of the trace neutrals involved, only one negative ion composition measurement has so far been reported. Furthermore, the D-region measurements from which one could could draw guidance are relatively sparse and somewhat ambiguous at present. Thus, our present understanding of the negative ion processes in the stratosphere stems largely from laboratory studies.

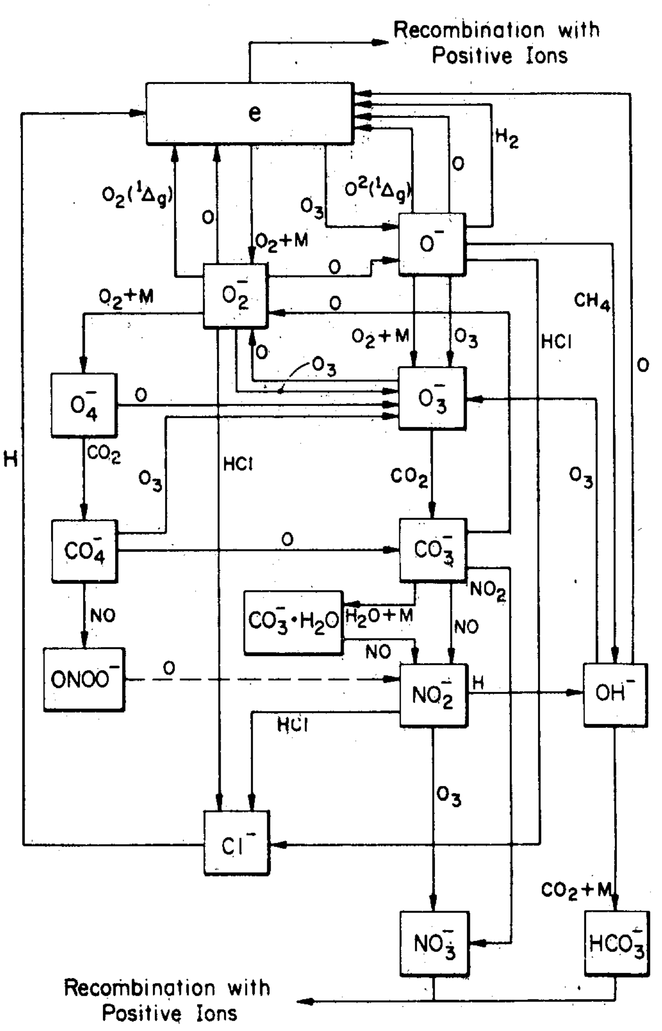

Figure 20-13. Reaction scheme of D-region negative ion chemistry [Ferguson, 1979].

The approach of Ferguson [1979] has been to start with the D-region negative ion chemistry given in Figure 20-13 and modify it to be in accordance with the expected differences in neutral composition of the two regions. Then one must look first for possible changes in the chemistry that leads to the NO_3^- ions and then consider whether these ions would react with trace neutral species that are suspected in the lower atmosphere to form even more stable ions.

The first necessary modification of the D-region scheme is to disregard the reactions of atomic oxygen, whose concentration below 50 km is negligible in comparison to that of O_3. In addition, NO will no longer play a role. Furthermore, the rapid formation of cluster ions can strongly alter the evolution of ion chemistry. For example, the reaction of O_3^- with CO_2 is known to decrease rapidly with O_3^- hydration. Because H_2O bonds more strongly to O_3^- than to CO_3^- this reaction may become endothermic when O_3^- becomes heavily hydrated. In the lower atmosphere, O_3^- hydration is likely to occur before the reaction of O_3^- with CO_2.

The reaction scheme based on these considerations is shown in Figure 20-14. The dashed lines represent places of considerable uncertainty. For example, it is not clear whether $O_2^- \cdot nH_2O$ ions will react with O_3, as do the unclustered O_2^- ions. The situation with $O_3^- \cdot nH_2O$, O_3^-, and CO_2 is the same; namely, the hydrated ions may not follow the same reaction paths as the unhydrated ions.

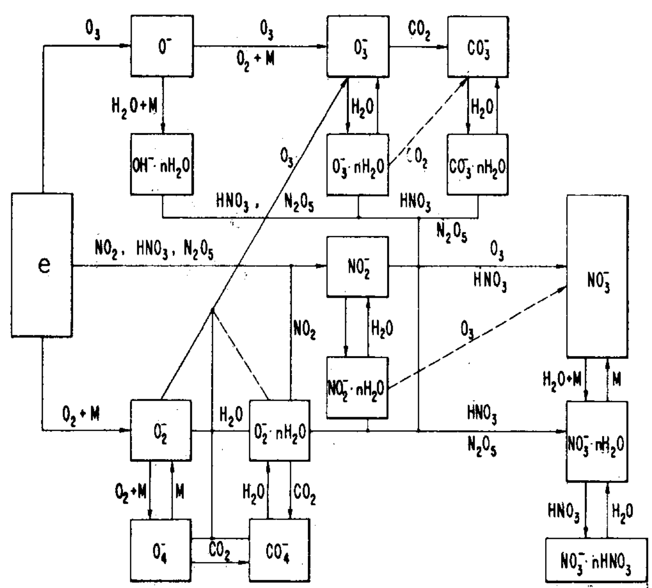

Figure 20-14. Stratospheric and tropospheric negative ion chemistry [Ferguson et al., 1979].

However, even if the paths that lead to NO_3^- are somewhat uncertain, its eventual formation does not appear to be in doubt. Both HNO_3 and N_2O_5 provide effective NO_3^- production routes. It is highly likely that the terminal negative ions of the lower atmosphere are complex cluster ions such as $NO_3^- \cdot \ell H_2O \cdot mSO_2 \cdot nHNO_3$, with NO_3^- as the core ion. Recently, middle atmosphere ions have been tentatively identified as $NO_3^-(HNO_3)_n$ and $NO_3^-(HCl)(HNO_3)_n$ with n = 1, 2, 3 in each case, as well as some ions which may possibly involve HSO_4^- cores and H_2SO_4 neutrals. Our understanding of the negative ion chemistry of the middle atmosphere is clearly in a rather elementary state.

20.1.5 Electrical Equilibrium and Variations

20.1.5.1 Electrical Equilibrium. Above the exchange layer in fair weather areas, the charged and uncharged nucleus content is low. To a first approximation, ion equilibrium exists. Assuming charge neutrality, Equations (20.14) and (20.15) reduce to

$$q = \alpha n_\pm^2. \qquad (20.25)$$

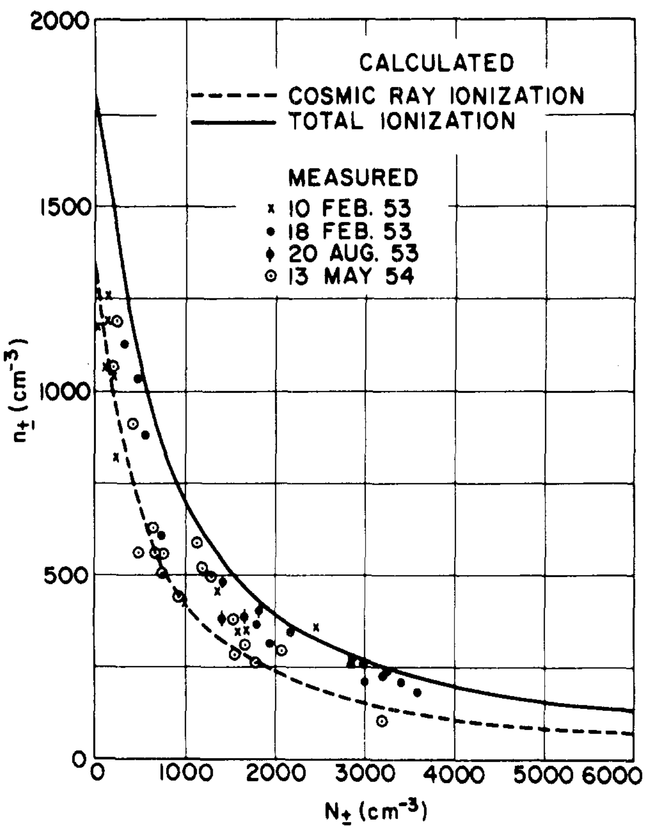

Figure 20-15. Positive or negative small ion number density n ± vs positive or negative charged nucleus concentration, N ± at 1.5 km altitude [Sagalyn and Faucher, 1956].

Measured values of production rates due to cosmic rays at various atmospheric depths and geomagnetic latitudes are given in Chapter 6.

Under equilibrium conditions in regions of significant nucleus concentration, Equations (20.14) and (20.15) reduce to

$$q = \alpha n_\pm^2 + n_\pm (\eta_{12} N_\pm + \eta_{10} N_o), \qquad (20.26)$$

or

$$n_\pm = -\frac{[\beta N_\pm \pm (\beta^2 N_\pm^2 + 4 \alpha q)^{1/2}]}{2 \alpha} \qquad (20.27)$$

where $\beta = \eta_{12} + \eta_{10}(N_o/N_\pm)$, and $N_\pm$ is the charged nucleus concentration of either sign. The dependence of small-ion density and conductivity on charged nucleus concentration computed for several altitudes is given in Figure 20-16. Figure 20-15 compares theoretical relations [Equation (20.27)] with experimental data for small ion content and charge nuclei concentration at 1.5 km. The good agreement between the theoretical curves and experimental data indicates the relation between small ions and nuclei is well understood.

20.1.5.2 Variations in the Exchange Layer. The exchange layer varies in depth between 0.15 and 3.0 km above the surface. Large variations in the electrical properties oc-

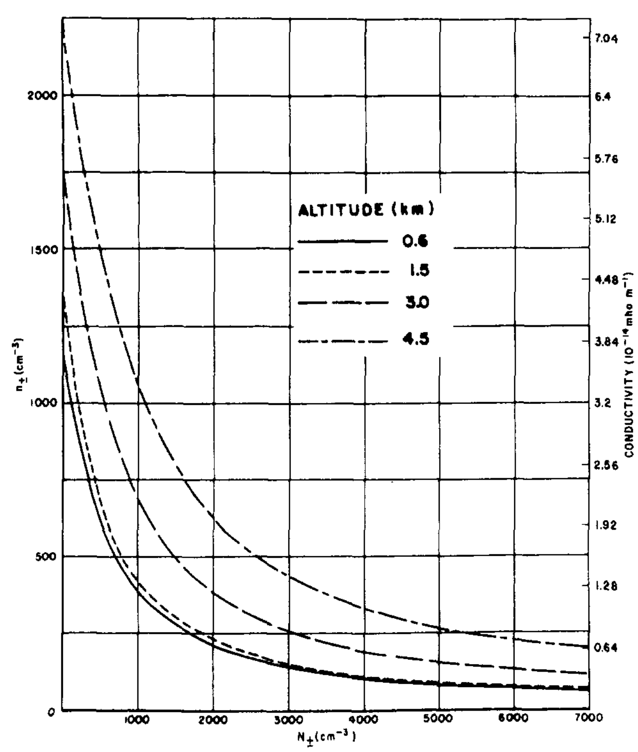

Figure 20-16. Positive or negative small ion number density η ± vs positive or negative charged nucleus concentration, N ± at 1.5 km altitude [Sagalyn and Faucher, 1956].

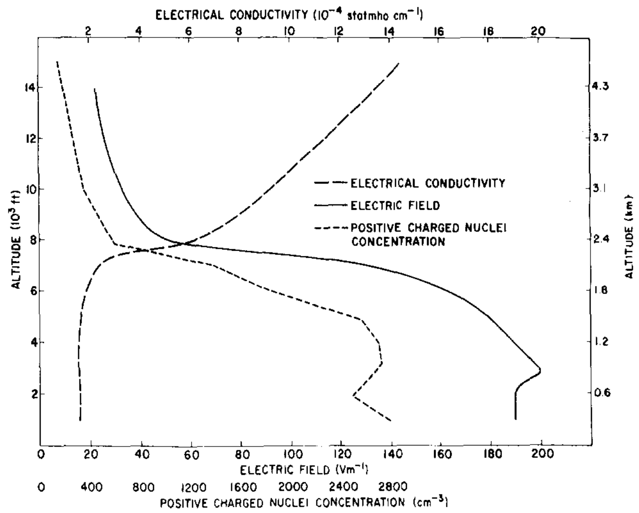

Figure 20-17a. Simultaneous values of electrical conductivity, electric field, and positive charged nuclei concentration vs altitude observed on 20 August 1953, 1311 to 1416 Eastern Standard Time [Sagalyn and Faucher, 1954].

cur in this layer. Meteorologically, the layer is characterized by uniform specific humidity and a nearly adiabatic temperature gradient rate at the upper boundary. The horizontal wind velocity differs from the wind velocity in the general circulation due to the frictional influence of the earth's surface. Figures 20-17a and b illustrate the variations of electrical properties with altitude in a well developed exchange layer.

The distribution and magnitude of the electrical properties vary from day to day and with time of day. During periods of low advection, regular daily variations can be observed. Figures 20-18a, b, and c demonstrate the daily variations observed during a series of aircraft flights over southern New Hampshire. The diurnal variation of the elec-

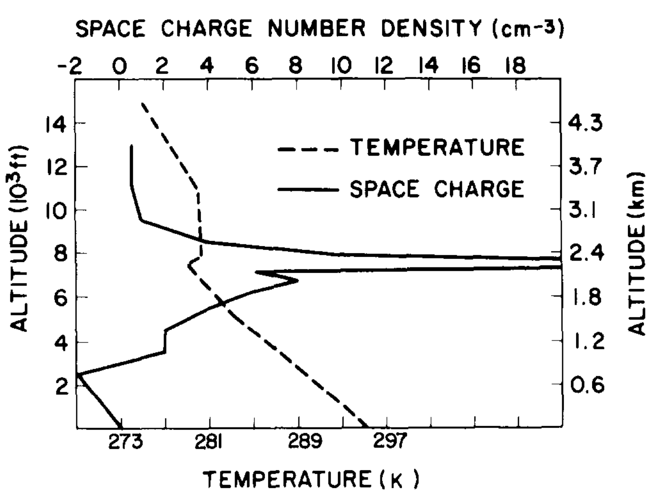

Figure 20-17b. Simultaneous temperature and space charge density vs altitude on 20 August 1953, 1311 to 1416 Eastern Standard Time [Sagalyn and Faucher, 1954].

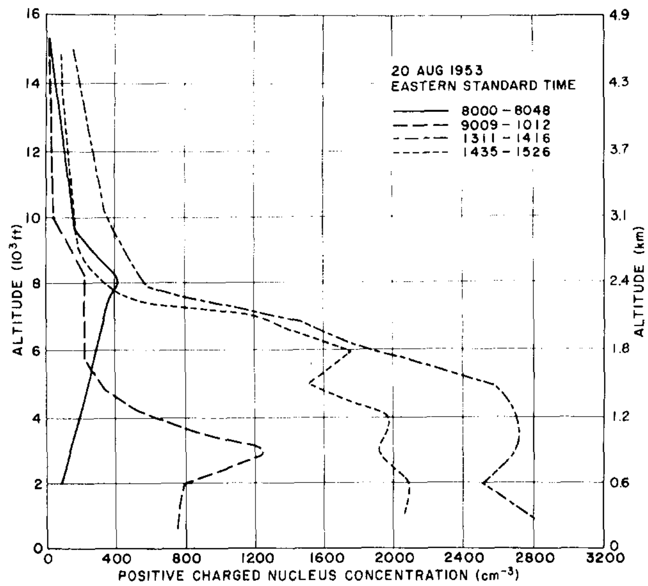

Figure 20-18a. Altitude and time variation of positive charged nucleus concentration during a period of low advection over southern New Hampshire [Sagalyn and Faucher, 1956].

trical properties illustrated in these figures results from the daily variation of the intensity of atmospheric turbulence and the influx of nuclei from the surface. Figure 20-19 shows the average daily variation in the columnar resistance of the atmosphere.

Over land areas, the most complicated distribution of the electrical properties is found between the surface and

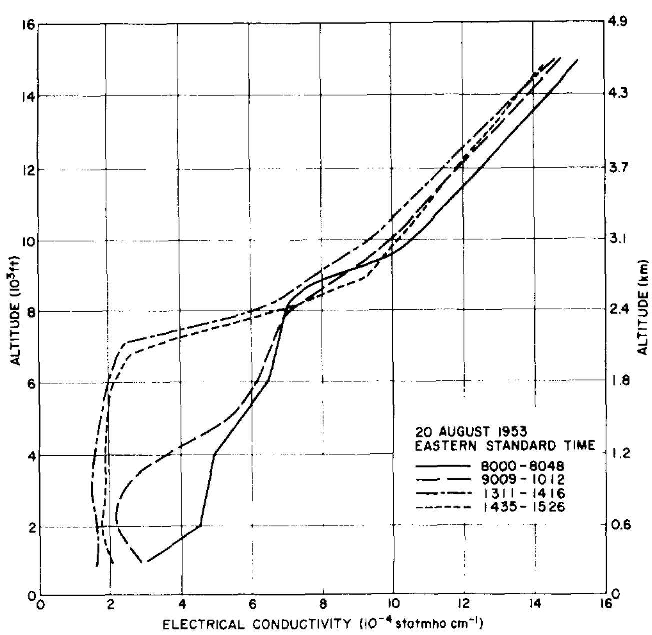

Figure 20-18b. Altitude and time variation of total volume conductivity during a period of low advection over southern New Hampshire [Sagalyn and Faucher, 1956].

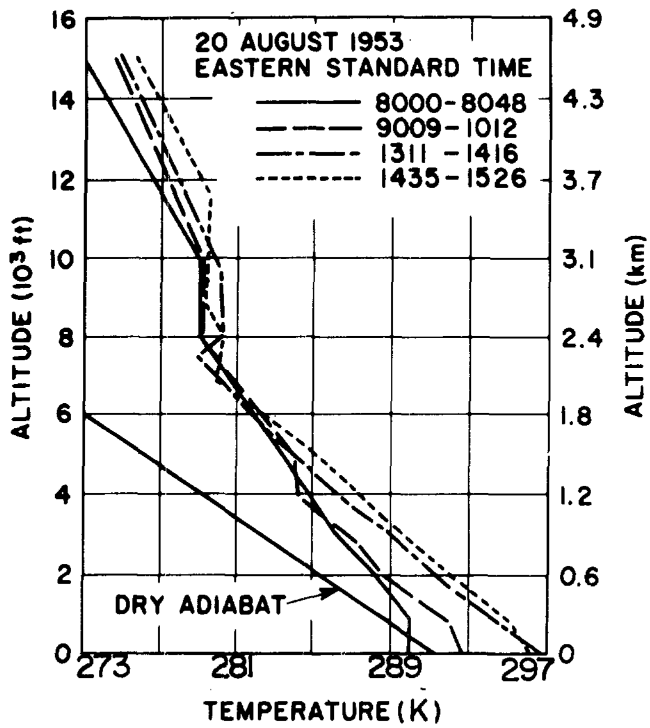

Figure 20-18c. Altitude and time variation of temperature during a period of low advection over southern New Hampshire [Sagalyn and Faucher, 1956].

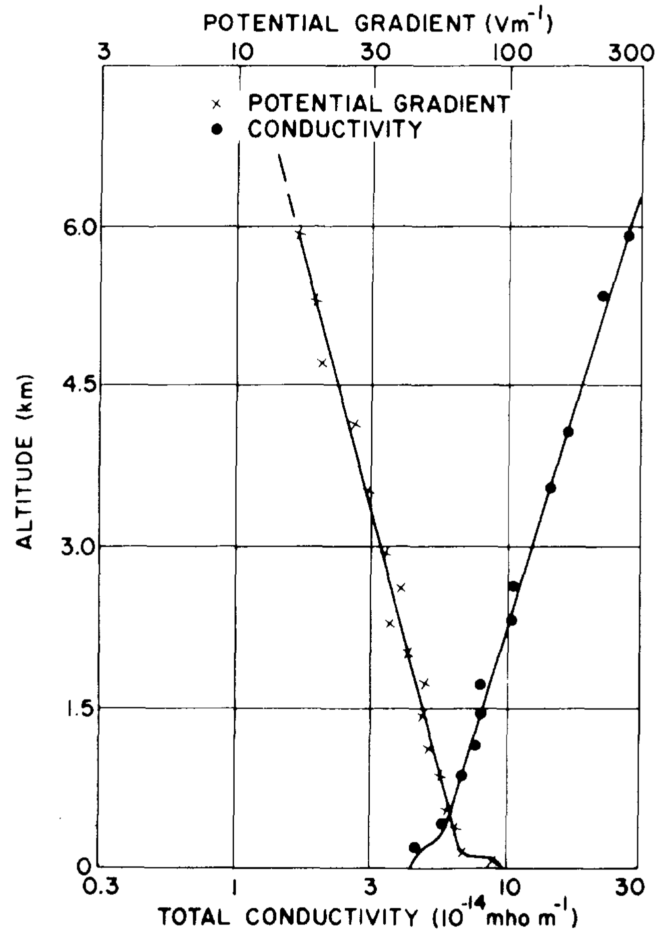

Figure 20-20. Electrical conductivity and electric field as a function of altitude over Greenland. (After J.F. Clark and J.M. Kraakevik [Smith, 1958].)

approximately 0.3 km. In this region ionization produced by radioactive emanations from the surface of the earth can, particularly in the early morning hours, cause an initial decrease of conductivity with height. This causes the potential gradient to increase with altitude and produces a negative space charge region near the ground. With the onset of turbulence, the concentration of ions in the region between the surface and 0.3 km is greatly reduced, and the conductivity increases or remains constant with altitude. In accordance with Poisson's equation, the potential gradient then decreases with altitude, and a positive or zero space charge exists in this region. The exact nature of the diurnal variation depends upon the radioactive content and porosity of the surface and on the intensity of atmospheric turbulence.

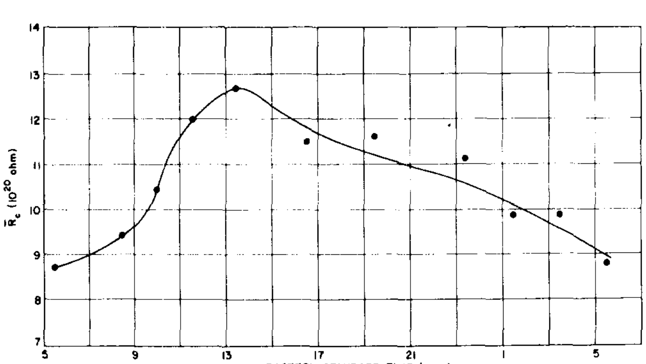

Figure 20-19. Diurnal variation of average resistance air column R_c of 1-cm^2 cross section and 4.6 km height [Sagalyn and Faucher, 1956].

The influence of the exchange layer on the electrical properties is minimal in regions where air masses are forming, such as the arctic and antarctic. This is illustrated in Figure 20-20 where the vertical distribution of electrical conductivity and the electric field measured on an early morning flight over Greenland are shown. Over oceans in high-pressure areas where very stable exchange layers are formed, negligible diurnal variation of the electrical properties are found. This is partly due to the absence of radioactive emanations from the surface and to a stable nuclei source. Examples of the electrical properties in a stable exchange layer over the oceans are shown in Figure 20-21a,b,c and d. Figure 20-22 shows the influence of the exchange layer on conductivities observed in mountainous regions.

20.1.5.3 Variations in the Free Atmosphere. The variability of the electrical quantities in fair weather in the troposphere is largely due to influences discussed throughout this

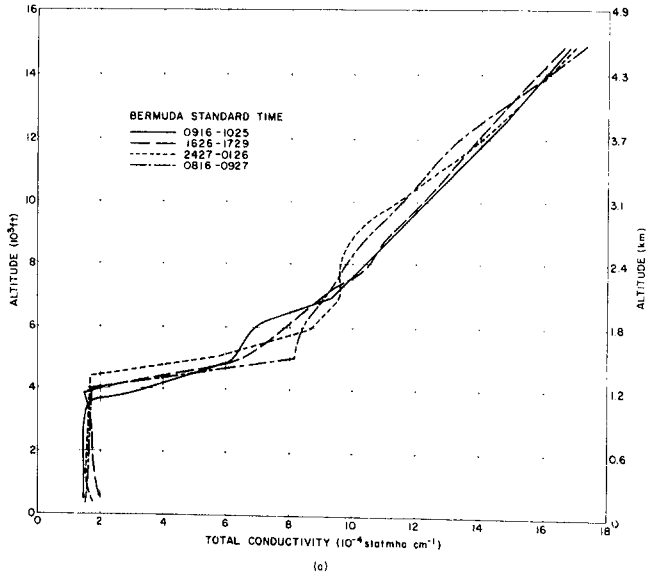

Figure 20-21a. Time variation of total electrical conductivity, positive charged nucleus concentration, temperature, and absolute humidity over the Atlantic Ocean at latitude 33°, longitude 64° on 13–14 April 1954. (From R.C. Sagalyn [Smith, 1958].)

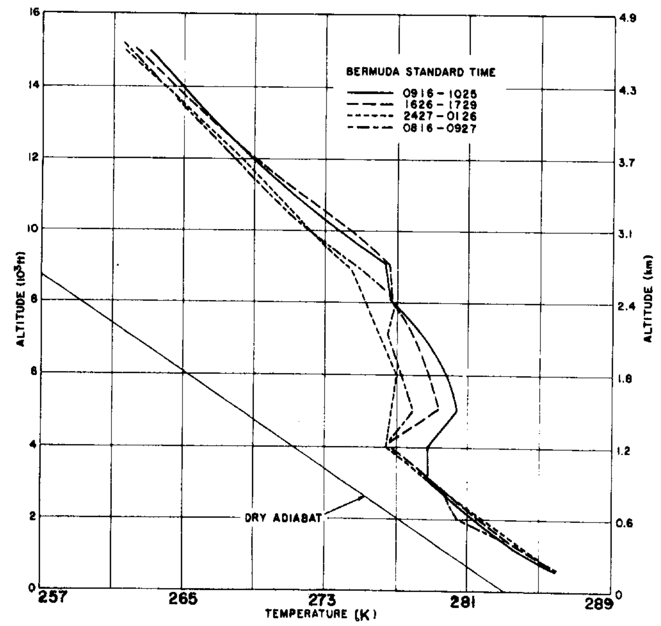

Figure 20-21c. Time variation of total electrical conductivity, positive charged nucleus concentration, temperature, and absolute humidity over the Atlantic Ocean at latitude 33°, longitude 64° on 13–14 April 1954. (From R.C. Sagalyn [Smith, 1958].)

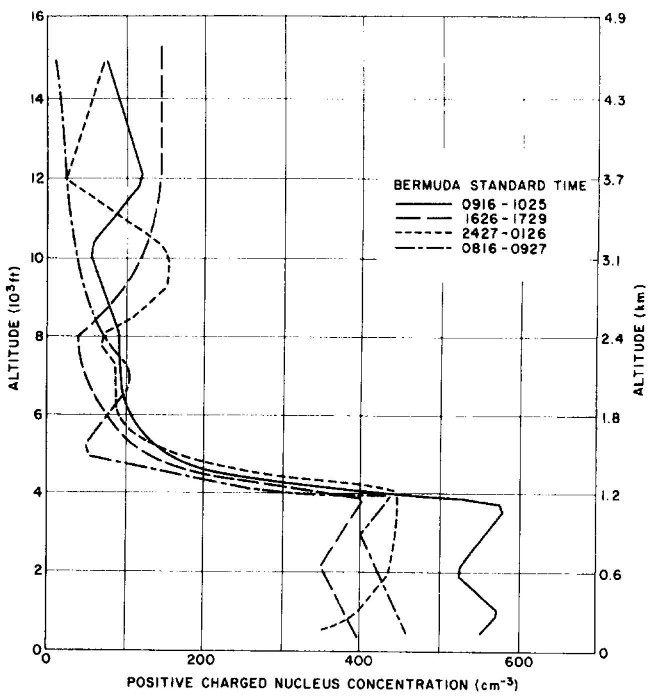

Figure 20-21b. Time variation of total electrical conductivity, positive charged nucleus concentration, temperature, and absolute humidity over the Atlantic Ocean at latitude 33°, longitude 64° on 13–14 April 1954. (From R.C. Sagalyn [Smith, 1958].)

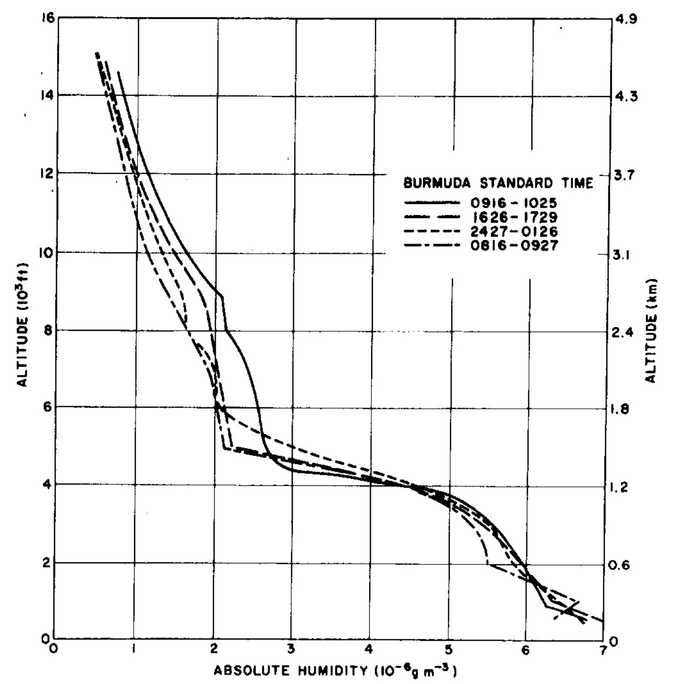

Figure 20-21d. Time variation of total electrical conductivity, positive charged nucleus concentration, temperature, and absolute humidity over the Atlantic Ocean at latitude 33°, longitude 64° on 13–14 April 1954. (From R.C. Sagalyn [Smith, 1958].)

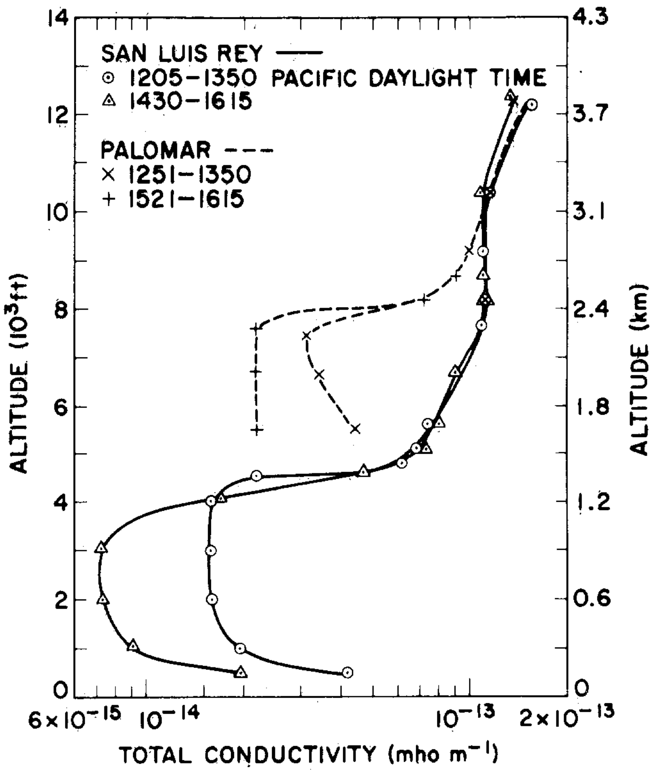

Figure 20-22. Electrical conductivity vs altitude over San Luis Rey station at 0.15 km and Palomar staton at 1.7 km on 8 June 1953.

chapter. For example, the variations in electrical conductivity both from model computation and measurements have been shown in Figures 20-3, 20-4, 20-18b, and 20-21. Those for the electrical field were demonstrated in Figures 20-7a, 20-7b, 20-17a, and 20-20. For conduction current, the variations were shown in Figures 20-8 and 20-9. Figure 20-5 was an example of the variations with altitude of small ion density. It is further demonstrated in Figure 20-23 [Sagalyn, 1965]. The variability of large nucleus concentration with altitude is shown

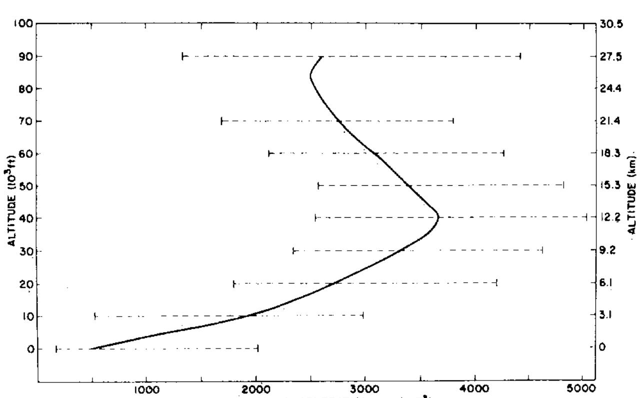

Figure 20-23. Average value and maximum variation of a small-ion density as a function of altitude. Data is based on over 60 aircraft flights throughout the eastern U.S.

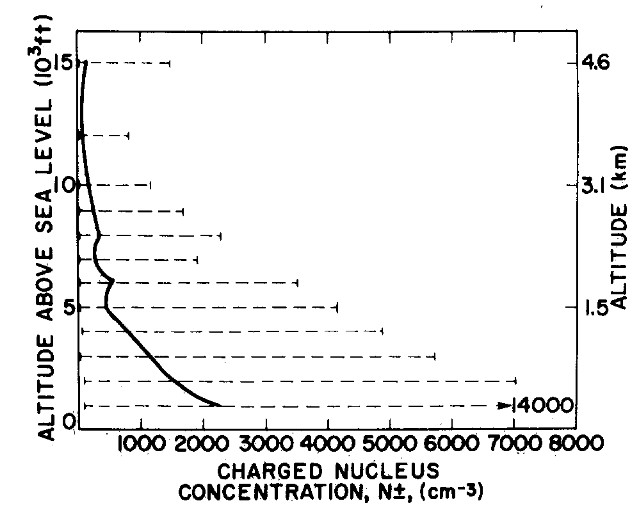

Figure 20-24. Average value and maximum variation of charged nucleus concentration as a function of altitude. Data is based on over 60 aircraft flights throughout the eastern U.S.

in Figure 20-24 [Sagalyn, 1965]. These results were obtained from over 80 aircraft and balloon flights throughout the U.S.

20.1.6 Solar Influence on Earth's Atmospheric Electrical Parameters

The connection between solar activity and the earth's atmospheric electrical properties and meteorological conditions is not yet understood. Investigations are underway to determine whether solar emission can act as a trigger mechanism for climatic changes over decades or millennia. Existing evidence strongly suggests a genuine link between transient energy-generating processes on the sun and electrical-meteorological responses in the near earth environment. The strongest effects are observed in the Northern Hemisphere winter when solar insolation is least effective, at middle to high latitudes [Herman and Goldberg, 1978a].

One way in which solar activity can couple into the atmospheric electrical system is through changes in the ion-pair production rate. Variations in atmospheric ionization and therefore in conductivity (except very near the surface) are produced by variations in the galactic cosmic ray flux intensity and by solar proton events.

Variations of the average ground-level cosmic ray intensity with the 11-year sunspot cycle are well documented and show a clear inverse correlation [Forbush, 1954]. An example of this is given in Figure 20-25 in which the normalized neutron monitor count rate from Climax, Colorado, is compared with average monthly Zurich sunspot numbers over two solar cycles. There is an approximate 20% decrease in count rate from solar maximum year 1957 to minimum year 1968. Data from Kent and Pomerantz [1971] indicate that at middle latitudes (55° geomagnetic) the count rate is

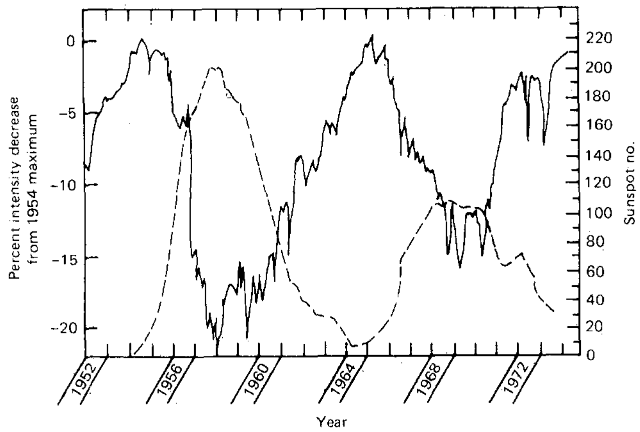

Figure 20-25. Solar cycle variation of cosmic ray intensity (solid curve) and sunspot number (dashed curve) over two solar cycles [Fulks, 1975].

about 21% lower at solar maximum, but near the equator is only 7% lower. The Climax cosmic ray intensity peaks approximately two-thirds of a year later than the time of sunspot minimum, but the amount of lag seems to be slightly different at different stations [Fulks, 1975].

The secular trend of potential gradient measured at stations in the British Isles, France, and Spain over a 20-year period (1902–1922) was investigated by Bauer [1926]. The average potential gradient for all stations combined, expressed in percentage of the 20-year mean value, was clearly above the mean during sunspot maximum years and below the mean in minimum years (Figure 20-26). For the potential gradient averages, days with local thunderstorms were excluded. Both the diurnal amplitude and the annual amplitude show a strong positive correlation with sunspot number over the two solar cycles. More recently, Muhleisen [1971] and Fischer and Muhleisen [1972] investigated the 11-year cycle influence on ionospheric potential. Their results also indicate a positive correlation with annual mean sunspot number.

Figure 20-12 shows the ion-pair production rate as a function of height for solar radiation (curves 1 to 5) and galactic radiation (curves 6 and 7). Although galactic cosmic rays carry more energy per particle and penetrate deeper into the lower atmosphere, episodic solar emissions and the related interplanetary magnetic field (dependent on flare activity and solar rotation) can produce higher ion-pair production rates in the lower atmosphere. This is demonstrated in curves 1 to 5 in which injections of solar protons during solar flares produce ionization above 20 km considerably in excess of the normal quiet background production rate provided by galactic cosmic rays in both sunspot minimum (curve 6) and sunspot maximum (curve 7) years. Curves (6 and 7) from Webber [1962] demonstrate the solar cycle variation in cosmic ray ion production at a magnetic latitude of about 70°.

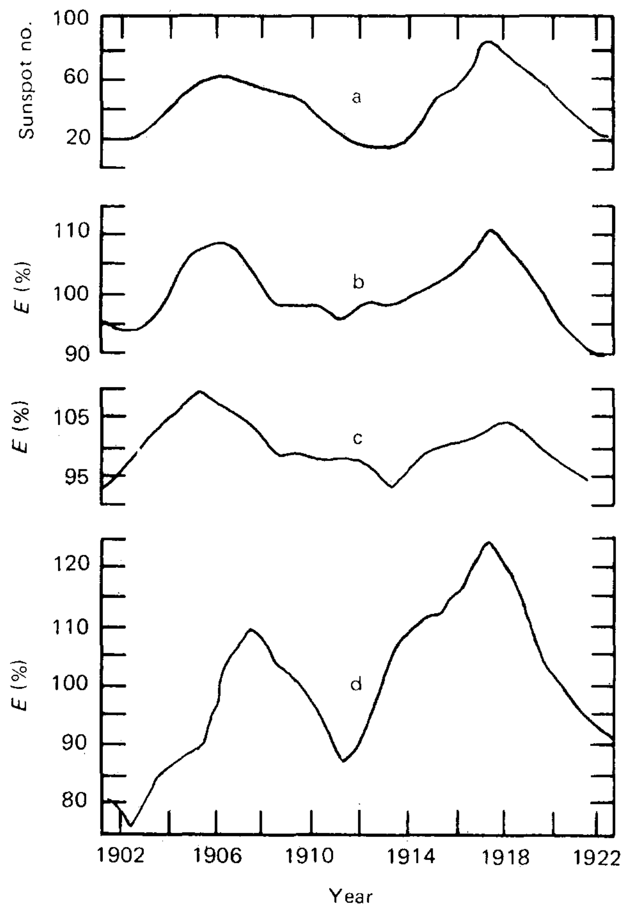

Figure 20-26. Cyclical variations in potential gradient compared to 11-year sunspot cycle. Curve a, relative sunspot number; b, potential gradient; c, daily amplitude of potential gradient; d, potential gradient annual amplitude. Curves b, c, and d are in percentage of mean values [Bauer, 1926 and Israël and Dolezalek, 1973].

On shorter time scales, solar flare eruptions and solar magnetic sector boundary crossings that result in increased numbers of solar protons entering the lower atmosphere also cause a decrease in galactic cosmic rays. The decrease in galactic cosmic rays following a solar flare is termed a Forbush decrease. From long term investigations, it appears that air-earth current, potential gradient, ionospheric potential, and thunderstorm activity all respond to solar flares. Enhancements in these atmospheric electrical quantities occur 1 to 4 days after the eruption of a major solar flare, with thunderstorm occurrence responding slowest. The increases range from 12% [Cobb, 1967] to 50% [Reiter, 1969] in air-earth current density, 30% to 60% in potential gradient [Reiter, 1969], and 20% [Flohn, 1950] to 70% [Bossolasco et al., 1972] in thunderstorm occurrence frequency.

The responses of atmospheric electrical quantities to solar flare occurrence are probably due to a combination of factors. High energy solar protons emitted during flares produce enhanced atmospheric ionization and thus increased conductivity above ~20 km altitude. The Forbush decrease in cosmic ray intensity following flares results in a decreased conductivity below 20 km altitude. These changes could lead to an increase in the electric field at levels below 20 km and a decrease above 20 km. This in turn can produce the potential increase observed during thunderstorm activity [Herman and Goldberg, 1978b].

20.1.7 Global Model of Atmospheric Electricity

Significant advances in the understanding of atmospheric electrical processes during the past decade have resulted from the development of global modeling and from inclusion of coupling with the ionosphere and outer atmosphere. Previously, atmospheric electrical phenomena were assumed to take place within a "concentric spherical capacitor" [Chalmers, 1967]. The lower boundary of this capacitor was the earth's surface and the electrosphere (a highly conducting layer at about 50–70 km) was assumed to be the upper boundary. The electrosphere is defined as the height of an equipotential that acts as a perfect electrostatic shield to physical processes taking place outside this region. Thunderstorms and other electrical processes in the lower atmosphere would then have no effect outside the electrosphere. Conversely, processes taking place beyond the ionosphere were assumed to have a negligible effect on electrical conditions in the lower atmosphere. In this view, thunderstorm activity was the major source of charge generation within the atmospheric electrical system and was balanced by the fair weather conduction current.

This "close-in" theory of atmospheric electricity is correct to first order in most cases. However, it does not allow for horizontal electric fields that are known to exist in disturbed weather areas and for variation in ionosphere characteristics. Recent studies indicate that the electrosphere is not a perfect equipotential layer. The "capacitor" is in fact leaky, with the result that atmospheric electrical processes interact with ionospheric and magnetospheric phenomena.

Hays and Roble [1979] derived a quasi-static numerical model of global atmospheric electricity in which thunderstorms are the main source of electric current. Thunderstorms are assumed to be distributed geographically in accordance with the known statistical distribution of thunderstorm frequency. In the model, the electrical conductivity increases exponentially with altitude and electrical effects are coupled into the magnetosphere along geomagnetic field lines. The electrical conductivity is assumed to vary with latitude, simulating the latitudinal variation of known cosmic ray production. The global distribution of electric potential and current is then calculated. The results show that large positive electric potentials are generated over thunderstorms and that these perturbations penetrate upward to ionospheric altitudes. The effect of a thunderstorm in one hemisphere can be transmitted along geomagnetic field lines into the conjugate hemisphere; however, the potential perturbation in the conjugate hemisphere is damped below stratospheric altitudes. Electric fields over thunderstorm regions may approach 0.25–0.50 mV/m at ionospheric heights for nighttime conditions. The return current at the earth's surface in the fair weather region is greater over mountainous regions than at sea level. The perturbation of the calculated electric potential and current distributions due to an increase in cosmic rays during a solar flare increase and the subsequent Forbush decrease in cosmic ray ionization can also be carried out using the model. An example of the output of the model is shown in Figure 20-27. The results in Figure 20-27 were derived assuming Northern Hemisphere summertime background with 2000 individual thunderstorms acting at 1900 UT. The vertical component of the electric field and the conduction current at the earth's surface are shown. Equipotential curves and constant current density contours are plotted in panels a and b, respectively.

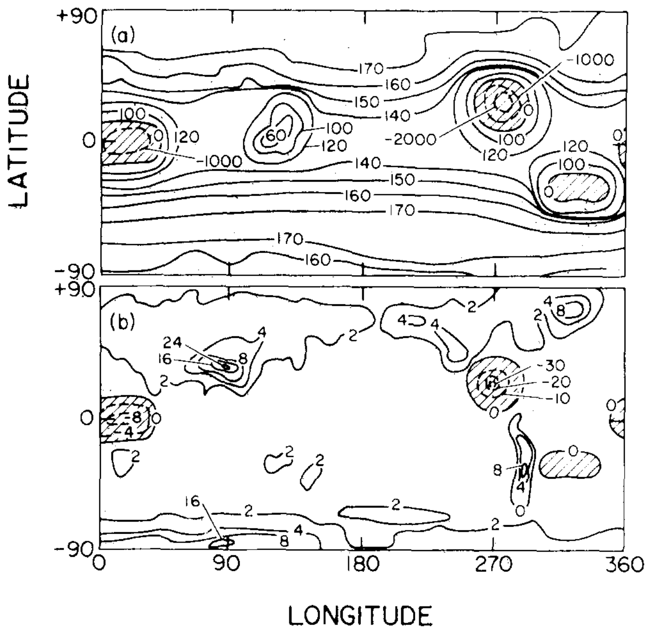

Figure 20-27. Results from Hays-Roble global atmospheric electricity model (a) latitude and longitude variation of the vertical component of electric field at the earth's surface (b) latitude and longitude variation of conduction current at the earth's surface [Hays and Roble, 1979].

20.1.8 Recent Advances in the Middle Atmosphere

20.1.8.1 Middle Atmosphere. The term "middle atmosphere" is used to describe the region between the tropopause and the mesopause, with possibly a slight extension into the lowest part of the thermosphere, that is, the altitude region 10 to 100 km. It includes the stratosphere and the meso-

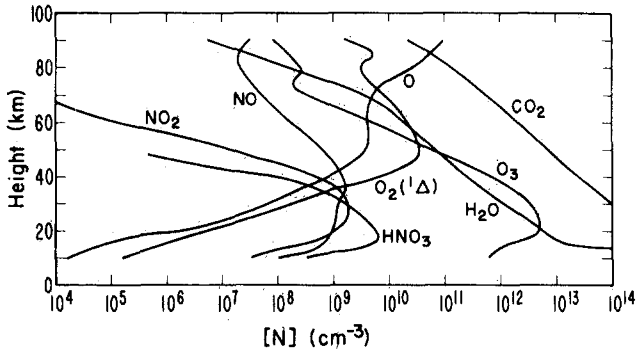

Figure 20-28. Typical daytime concentration profiles of some minor constituents of the middle atmosphere [Reid et al., 1979].

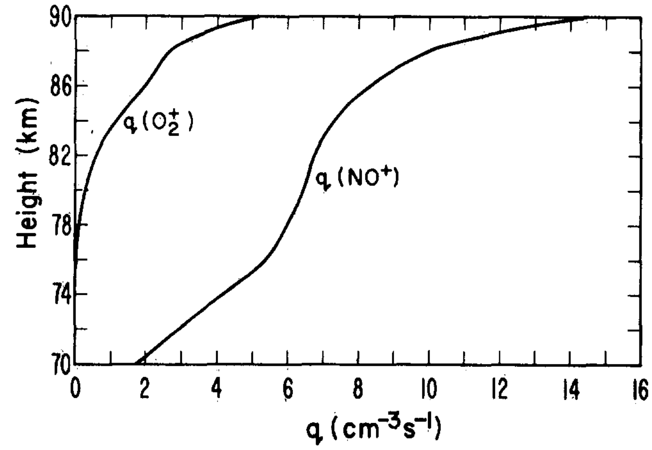

Figure 20-29. Rate of ion production for a solar zenith angle of 45° and undisturbed conditions [Reid et al., 1979].

sphere, knowledge of which has increased greatly as a result of recent studies of the ozone layer (Chapter 21).

Knowledge of the chemical composition is fundamental to the understanding of the electrical characteristics of the middle atmosphere. Several minor constituents, typical profiles of which are shown in Figure 20-28, play prominent roles. The composition of the middle atmosphere was discussed in Section 20.1.4. The temperature structure and the wind systems of the middle atmosphere are determined by a balance between the heating and cooling rates. The heating is due primarily to the absorption of solar radiation by ozone, and the cooling to infrared radiation, mainly by carbon dioxide. Thus, these two minor constituents determine the structure of the middle atmosphere. The other constituents shown in Figure 20-28 are the chief participants in the production of ionization, or in the ion chemistry that determines the steady-state ion concentration and composition.

During the winter, there is a pronounced equatorward-directed temperature gradient in the middle atmosphere, and the resultant geostrophic winds are westerly as in the troposphere. Wind speeds reach their maximum near the stratopause, forming the so-called polar-night jet, surrounding a strong polar vortex. During the summer the situation tends to be reversed, with a poleward-directed temperature gradient caused by the combination of a high-latitude ozone maximum and essentially continuous insolation, giving rise to prevailing easterlies throughout most of the middle atmosphere. The spring and fall transitions between these two average conditions and major transient stratospheric warming events of the late winter are periods of particular interest in the middle atmosphere.

Vertical transport in the middle atmosphere is usually parametrized through the use of an eddy-diffusion coefficient whose profile is based on observed vertical diffusion rates. Characteristic vertical mixing times are long, varying from years in the lower stratosphere, to months in the upper stratosphere and lower mesosphere, and to weeks in the upper mesosphere. Since these are much longer than the characteristic lifetimes of ions, the ions are not themselves directly affected by vertical transport. Many of the minor species that determine the ion composition, however, are dominated by transport effects rather than by photochemistry in much of the middle atmosphere.

The major source of mesospheric ionization is the NO molecule, which can be ionized by solar Lyman-alpha radiation at 1216 Å. The Lyman-alpha line coincides with a window in the O_2 absorption spectrum and penetrates most of the mesosphere reaching unit optical depth at about 75 km for an overhead sun. NO^+ is the primary ion species produced by this source. Figure 20-29 shows the rates of production of both $O_2{}^+$ (from the $O_2(^2\Delta)$ source as well as from x-rays during average solar conditions) and NO^+ for a solar zenith angle of 45° and for currently accepted profiles for NO and $O_2(^1\Delta)$.

In the lower mesosphere and throughout the stratosphere, the chief source of ionization under normal conditions is galactic cosmic rays. The rate of ion production due to cosmic rays was shown in Figure 20-12 for different latitudes and solar conditions. The cosmic ray induced variation of small ion density with latitude is given in Figure 20-5.

The solar magnetic field and solar wind act to exclude cosmic-ray particles from the near earth environment through mechanisms that are not yet fully understood. The chief result is that the cosmic-ray flux at the earth is lower during solar maximum, when the solar magnetic field is more intense on the average, than during solar minimum. The inverse relation between solar activity and cosmic ray intensity near the earth's surface is illustrated in Figure 20-25. This produces a significant solar-cycle variation in the electrical properties of the middle atmosphere.

20.1.8.2 Middle Atmosphere Ion Concentration, Mobility, and Conductivity. The fundamental relations discussed in Sections 20.1.1 through 20.1.6 are valid throughout the middle atmosphere. The steady-state ion concentra-

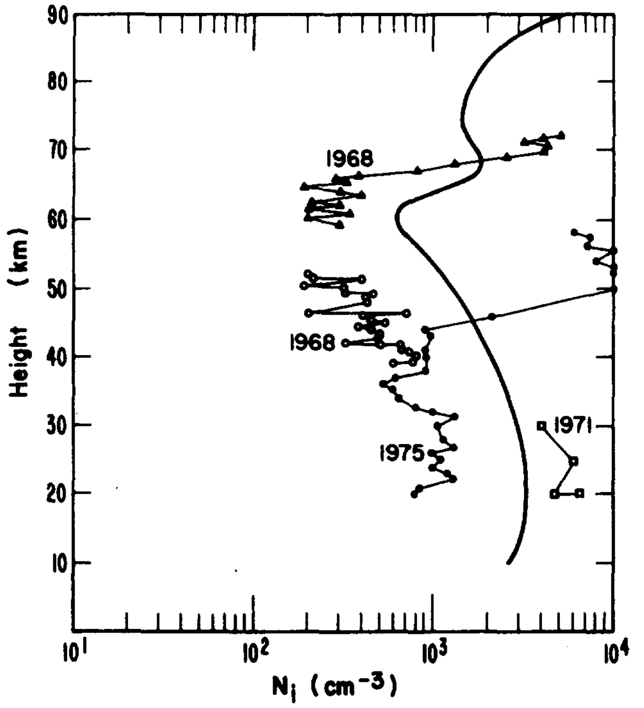

Figure 20-30. Positive-ion concentration profile from model calculation (solid line) and observed [Reid et al., 1979].

tion profile of the middle atmosphere is illustrated in Figure 20-30 which shows the results of a recent model calculation of positive-ion concentrations for solar-maximum year at geomagnetic latitude 40°, and for a solar zenith angle of 45°. Also shown in the figure are the results of direct measurements of small-ion concentrations for similar geomagnetic latitude but for different phases of the solar cycle. Obviously there is a general agreement in the shape of the profiles, but the sharp enhancements in ion concentration that appeared at 65 km in 1968 and at 45 km in 1975 have

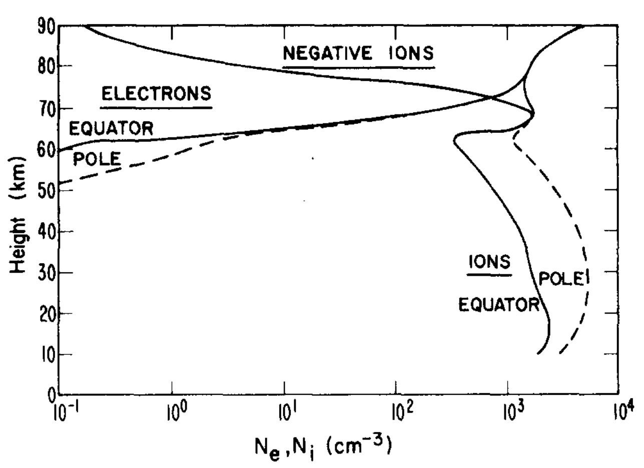

Figure 20-31. Negative ion and electron concentration profiles at the pole and equator from model calculation [Reid et al., 1979].

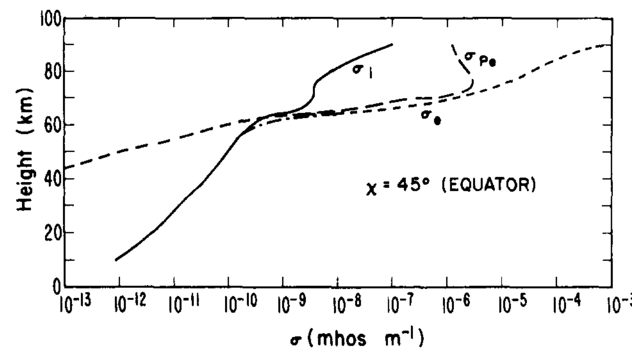

Figure 20-32. Calculated profiles of electron and ion conductivity at the equator. [Reid et al., 1979].

no counterpart in the theoretical results. The model results also appear to be higher by about a factor of three than the actual observations over most of the range. Since our knowledge of the ion production rate is unlikely to be seriously in error, at least below 60 km, the discrepancies must reflect our lack of knowledge of the full details of the ion chemistry of the stratosphere.

Figure 20-31 shows the results of a similar model calculation of the concentrations of the negatively charged species—negative ions and electrons—for the same conditions of solar illumination but for polar and equatorial latitudes. The very sharp transition between the overlying electron-dominated region and the underlying negative/positive-ion dominated region is the most obvious feature. There is considerable observational confirmation consistent with the model that the transition from negative ion to electron occurs at about 70 km during quiet daytime conditions.

Figures 20-32 and 20-33 show theoretical profiles of conductivity for equatorial and polar latitudes, again for solar maximum conditions and for a solar zenith angle of 45°. The solid lines represent the ionic component and the broken lines the electronic component of the conductivity, with the crossing points marking a sudden increase in the gradient of total conductivity. Below this altitude, substan-

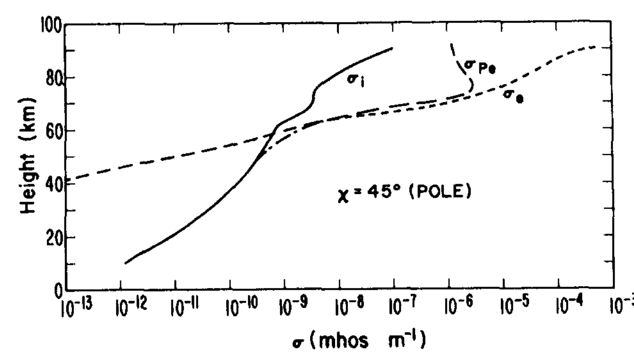

Figure 20-33. Calculated profiles of electron and ion conductivity at the poles. [Reid et al., 1979].

tial horizontal potential differences can be maintained, but the conductivity at higher altitudes is large enough to allow only relatively small potential variations on a global scale.

In the upper mesosphere the geomagnetic field begins to have an important effect on the electron conductivity. The electrons are forced to spiral about the magnetic field, and if the collision frequency is low enough they can no longer move freely along the direction of an applied electric field that has a component perpendicular to the magnetic field. Collisions with gas molecules, however, break up this organized spiraling motion, and allow some movement along the electric field direction, thereby preventing the electron conductivity along the direction of the electric field from vanishing entirely. The residual electron conductivity perpendicular to the magnetic field is referred to as the Pedersen conductivity, and is shown in Figures 20-32 and 20-33 by the broken line labeled σ_{Pe}. The conductivity along the direction of the magnetic field is unaffected by the spiralling motion of the electrons, and is identical to the uniform conductivity that would exist if there were no magnetic field. It is shown by the broken line labeled σ_e. Since the electrons drift along a direction perpendicular to both the magnetic and electric fields between collisions, there is a third component of the conductivity known as the Hall conductivity, but it differs in character from the other components by virtue of its vanishing power dissipation (since $j_H \cdot E = 0$). Throughout the middle atmosphere the ions remain collision dominated and are just as free to move perpendicular to the magnetic field as they would be in the absence of a magnetic field.

The various sources of middle-atmosphere ionization vary on a wide range of time scales, and a corresponding variability in the electrical parameters must exist. In the mesosphere, the solar x-ray flux varies with the 27-day solar rotation period, with the 11-year solar cycle, and with individual flares when its intensity can increase by at least three orders of magnitude above the normal value. Except during intense solar flares, x rays remain a fairly negligible ionization source.

The major mesospheric source of ionization of NO, Lyman-alpha, increases by nearly a factor of two from solar minimum to solar maximum and by about 30% in the course of a solar rotation. The concentration of NO will vary with the production of NO in the lower thermosphere by energetic particles. Auroral ionization is known to be accompanied by the production of large quantities of NO near 100 km altitude, but downward diffusion of NO into the mesosphere is still unknown.

The electrical properties of the middle atmosphere are highly complex and variable. The middle atmosphere responds to driving forces from above and from below, and is subject to electric fields of both tropospheric and magnetospheric origin. It must play a significant role in any solar terrestrial coupling mechanisms that involve the lower atmosphere.

20.2 THUNDERSTORM ACTIVITY

20.2.1 Thunderstorm Charge Distribution and Electric Field Pattern

The thunderstorm is the final product of the growth of a series of clouds with vertical development known in order of increasing size as cumulus, cumulocongestus, and cumulonimbus. This class of cumuliform clouds is formed through the upward transfer of energy from surface heating effects leading to buoyant vertical air motions or through the lifting effects associated with the motion of atmospheric frontal weather zones. The cumuliform clouds derive their energy from the latent heat of condensation and sublimation of atmospheric water vapor drawn into the cloud circulation. The intensity of the resulting convective activity depends on the available moisture and the stability of the lower atmosphere as expressed by the air temperature variation with height. Weather services technically distinguish the thunderstorm from other convective clouds by the observation of thunder. These storms normally are associated with extensive lightning activity, heavy rain showers, possible hail or snow pellets, and strong subcloud wind gusts due to the spreading out of cold downdrafts from the areas of precipitation.

The storm electrical activity is spectacular and dangerous; however, it represents an energy expenditure of less than 1% of the thermal, gravitational, and kinetic energy associated with the condensation of moisture and the development of drafts and precipitation [Braham, 1952]. The storm progresses through three stages of its life cycle. The growth stage is characterized primarily by in-cloud updrafts. The active stage is accompanied by cloud top glaciation or conversion to ice forms, and the presence of strong up and downdrafts, lightning, and precipitation. The dissipating stage is reached when a lifting or breaking up of the lower cloud and a layering and spreading out of the upper anvil or ice form cloud material occurs. At this point the vertical air motions are greatly reduced and the precipitation is reduced to widespread fairly uniform small droplets or small snowflakes falling from the anvil [Byers and Braham, 1949]. By this time the electrical activity has subsided. However, considerable residual electric charge remains stored on the cloud particles and there is a possibility of occasional strong cloud to ground lightning or of a strike to an aircraft or rocket entering the cloud.

Details of the electric charge generation process in storms are not fully established. Numerous observations indicate that strong electric fields and lightning are usually found in convective clouds that contain mixtures of water droplets and various forms of snow and ice particles. The charge is probably generated through a combination of processes involving differential small ion capture by water droplets, induction effects of collisions of different sized particles in an existing electric field, and physical effects. These include a tendency of water droplets to form an easily shattered electrical double layer in the droplet surface, possible proton migration in the ice crystal lattice structure due to thermal gradients, and other effects associated with the liquid to solid and solid to liquid phase changes which occur during the formation and fallout of precipitation.

Separation of the charge generated as a result of an enormous number of these microscale events is brought about primarily by the differential motion of variously sized precipitation and cloud particles due to gravitational forces and by the draft velocity production of aerodynamic drag forces on the particles. On the order of 1000 coulombs of bound space charge are produced and maintained during the late growth and active period of the storm. Observations indicate certain regions of the storm characteristically have an excess of negative or positive charge. These zones of unbalanced charge create electrostatic fields that extend to the surface of the earth and for a considerable distance into the clear atmosphere surrounding the storm. Measurements of these fields and of the field changes due to the neutralization of portions of the charge centers during lightning flashes were originated by Wilson [1916]. Numerous subsequent observations confirm that the electrical structure of the storm appears to resemble a bipolar charge distribution with an upper positive and lower more concentrated negative charge center. Some storms have an additional small positive center located near the cloud base. This center seems to be closely associated with the major rain shafts falling from the storm. A typical midlatitude storm is depicted in Figure 20-34. The charge center locations are more closely related to the vertical temperature structure than to the geometric differences in height of storms in various geographic areas of the world. The approximate temperature dependence is shown by the scale along the vertical axis. The estimated percentage frequency of lightning channel paths is given by the circled numbers adjacent to the various forms of lightning events depicted.

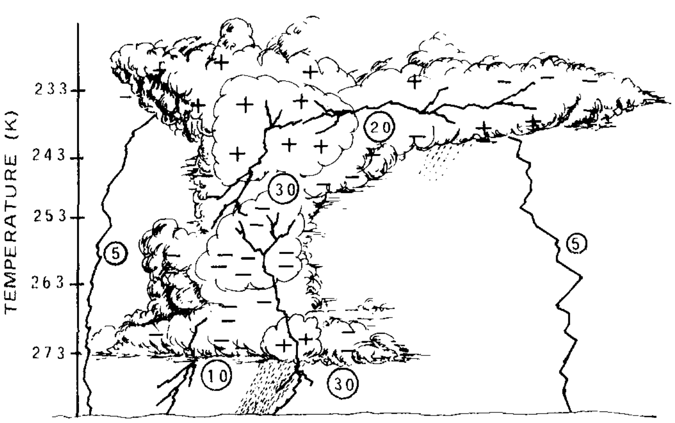

Figure 20-34. Typical charge distribution and lightning patterns of a midlatitude thunderstorm.

20.2.1.1 Surface Electric Field. The magnitude of the electric field of a thunderstorm as measured at ground level is strongly dependent upon local topography and the degree to which vegetation and structures are present to supply sources of point discharge current from the earth in response to the storm-initiated field. Storms over water and in mountainous terrain above timberline may produce maximum surface fields of about 100 kV/m. Storms moving over wooded, brushy or other terrain, which can provide numerous small pointed sources for development of a point discharge current, normally form a layer of space charge about 200 m thick near the ground under the storm. This layer acts to reduce the field at the ground to about 10 kV/m. Moving storms typically have some wind induced tilt to the main bipolar charge axis. This results in a wave like pattern in the time series observation of the surface field as a storm passes. Figure 20-35 indicates the general form and dimensions of the electrostatic disturbance

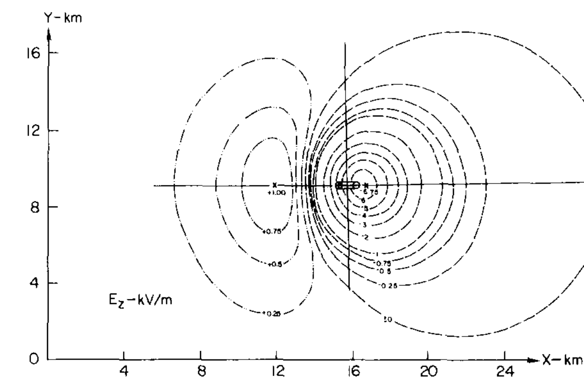

Figure 20-35. Electric field produced at surface of earth by the tilted bipole model [Fitzgerald, 1957].

associated with these storms. The figure is drawn for a lower 10 coulomb negative center at 3.5 km height and an upper 10 coulomb positive center at 4.5 km which is displaced down wind by 1 km. This figure indicates that the electric field at a particular site may exhibit a strong initial increase of field in either a positive or negative direction if a thunderstorm develops or moves into the vicinity. Interpretation of the time series field record for lightning warning is strongly dependent upon station location with respect to the cloud, the state of development of the cloud, and the structure of the winds aloft.

A typical pattern of the electric field associated with the passage from west to east of a squall line thunderstorm complex in the midwestern United States is shown in Figure 20-36. The initial rise in field associated with the approaching anvil charge is seen to the right of the figure. This is followed by a field reversal as the main-storm mass approaches the station. Numerous lightning field changes are indicated by the abrupt discontinuities in the basic wave

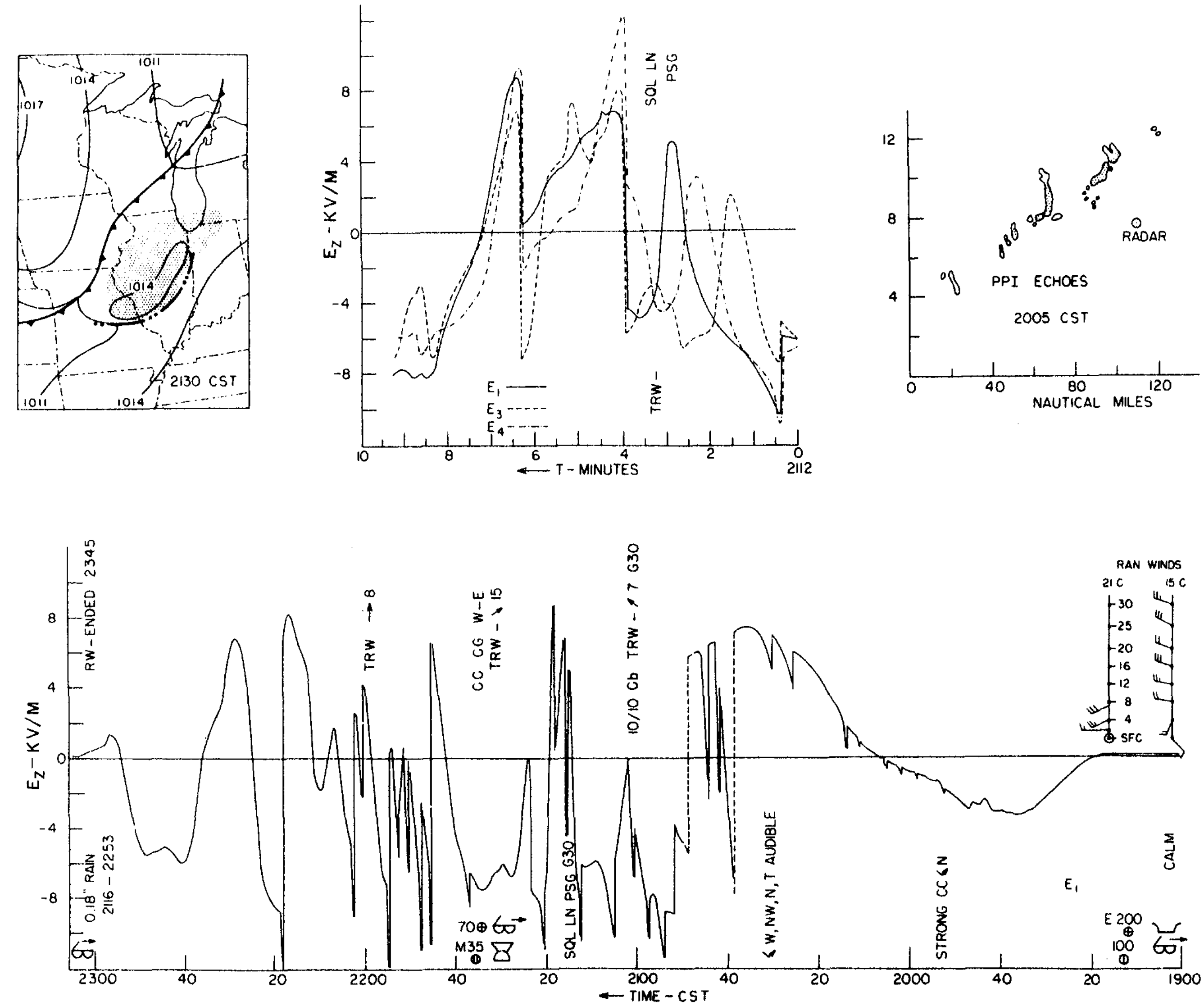

Figure 20-36. Surface field with active squall line passage, Illinois [Fitzgerald, 1956].

pattern. The squall line passage from 2115 to 2120 was accompanied by a lower positive charge region in the main part of the storm. Several subsequent alterations of lower negative and positive regions are noted as the storm passed the station. The final positive rise before return to the fair weather field was associated with the receding anvil structure. Some characteristics on the duration and lightning activity of typical slowly moving summer storms at Kennedy Space Center, Florida are given in Table 20-6 from a study by Livingston and Krider [1978]. These storms are frequently of long duration and large dimensions. They are accompanied by considerable lightning activity and heavy precipitation.

Jacobson and Krider [1976] have summarized magnitudes and altitudes of charge centers destroyed in lightning events studied in various geographical regions. Their summary is given in Table 20-7.

20.2.1.2. Field Patterns Aloft. Aircraft measurements indicate that electrostatic field components within storms are usually in the range of from 30 to 150 kV/m. Frequent alterations of polarity are found. These are usually associated with areas of differing precipitation forms, free air temperature, and vertical air motion. The scale of these complex field regions ranges from about 300 m to several km. Small intensely charged regions are occasionally found. These may have field components as high as 400 kV/m. These small regions are considered likely sources of lightning initiation.

The general pattern of the vertical component of the electric field in thunderstorms occurring in England was determined by Simpson, Scrase, and Robinson through a number of balloon soundings. Figure 20-37 adapted from Simpson and Robinson [1941] represents a summary of their results. It shows isolines of constant vertical field for a

Table 20-6. Summary of electrical behavior of 1975 and selected 1976 air mass storms at the NASA Kennedy Space Center [Livingston and Krider, 1978].

Date	Start/Stop Times, UT	Storm Duration, min	Total Number of Discharges	Maximum Flashing Rate, min^{-1}	Average Flashing Rate, min^{-1}	Maximum Radar Top, km
			1975			
May 15	1455/1608	73	533	20.0	7.3	14.0
June 2	1739/2004	145	866	17.0	6.0	13.7
	2002/2325	203	503	6.0	2.5	14.9
June 3	1702/1915	133	434	10.6	3.3	15.2
June 7	2011/2114	63	361	17.2	5.7	
	2202/2243	41	105	9.8	2.6	
June 9	1930/2350	260	879	10.4	3.4	15.5
June 10	2053/2127	34	25	1.2	0.7	10.1
June 16–17	2006/0105	299	1853	24.8	6.2	14.3
June 17	1514/1615	61	31	1.2	0.5	12.2
	1617/1745	88	79	1.4	0.9	12.2
	1753/1855	62	126	3.6	2.0	12.2
	1850/1926	36	74	4.0	2.1	12.2
June 18	1533/1709	96	122	3.6	1.3	12.2
June 20	1541/1605	24	8	0.4	0.3	8.2
June 26	2012/2230	138	579	9.2	4.2	15.8
June 27	1930/2021	51	178	6.8	3.5	
	2031/2300	149	1392	21.0	9.3	17.7
June 28	0000/0120	80	31	1.0	0.4	12.2
	0115/0145	30	18	1.0	0.6	
July 8	1831/2020	109	303	9.0	2.8	11.3
July 9	0000/0220	140	185	5.2	1.3	9.4
July 9–10	2037/0010	213	1943	24.0	9.1	16.5
July 10	1940/2325	225	1987	26.0	8.8	16.5
July 11	1714/1829	75	97	3.4	1.3	11.0
July 13	2001/2032	31	12	1.0	0.4	14.0
	2020/2232	132	96	2.0	0.7	14.0
TOTAL		2991	12820		4.2	
			1976			
July 8	1513/1543	30	47	7.0	1.6	
July 13	1725/1835	70	359	15.4	5.1	15.8

model containing +24 coulombs of upper charge, −20 coulombs of intermediate level charge and +4 coulombs of lower positive charge. The lower trace represents the field at the surface due to this model. The height and distance scale shown is typical of most European thunderstorm situations. United States and tropical area storms may have much larger dimensions. Later balloon soundings by Chapman [1958], Winn et al. [1981], Weber et al. [1982], and Rust and Moore [1974], for example, have been made in New Mexico storms. Parker and Kasemir [1982] have summarized the electrical structure of the lower regions of Colorado and Wyoming storms as measured by Kasemir and Holitza. Two aircraft equipped with electric field sensors were used to acquire data at two altitudes in the storm. A typical vertical field profile is shown in Figure 20-38. Chapman's [1958] balloon sounding had a generally similar shape. However, positions of the field maxima and zero crossover points were located about 500 m lower and the maximum fields inferred were about ±90 kV/m.

Combined cloud physics and electrical measurements of thunderstorm properties were conducted as a joint Air Force-National Severe Storms Project experimental program during the 1962–1966 time period. Figure 20-39 depicts the vertical electric field, voltage on the F-100F penetration air

Table 20-7. Summary of lightning charges, altitudes, and moment charges in various geographical locations. [Jacobson and Krider, 1976].

Geographical location	Charge (C)	Altitudes of lightning charges above local terrain† (km)	Range of air temperatures (K)	Moment changes (C · km)	Investigators
Florida	−10 to −40	6 to 9.5 (0)	263 to 239	100 to 600 400 (av)	present study
England	−11.5 to −46	7 (1)	239*	33 to 430	Wilson (1916)
England	−20	2 (1)	272.5*	100 (av)	Wilson (1920)
England	−10 to −40	4.5 to 5 (1)	257 to 254*	220 (av)	Wormell (1939)
England	—	—	—	150 (av)	Pierce (1955)
South Africa	−15	3 (1.8)	260*	93 (av)	Schonland (1928)
South Africa	−4 to −40	2.5 to 8.7 (1.8)	263 to 225*	41 to 495	Barnard (1951)
South Africa		4 to 8.5 (1.8)	266 to 235	—	Malan and Schonland (1951)
New Mexico	−24 (av)	4 to 7 (1.6)	268 to 248	—	Workman et al. (1942)
New Mexico	−5 to −20	4.3 to 7.2 (2.1)	266 to 240	—	Reynolds and Neill (1955)
New Mexico	−5 to −60	3 to 8 (1.8)	260 to 237*	249 (av)	Brook et al. (1962)
New Mexico	−30 to −48	4.5 to 6 (1.8)	270 to 250*	—	Krehbiel et al. (1974)
Japan	−50 to −150	4 to 8 (1)	269 to 248	—	Hatakayama (1958)
Japan	−6 to −55	6 to 8 (1)	262 to 249*	—	Tamura (1954)
Japan	−20 (av)	3.5 to 5.5 (1)	276 to 265*	—	Takeuti (1966)
Hong Kong	−25 (av)	4 (1)	272*	210 (av)	Wang (1963)
Australia	−17 (median)	3 (median) (1)	278*	150 (av)	Mackerras (1968)

*Estimated temperatures using climatological averages for the month of interest [U.S. Department of Commerce, 1971].
†The numbers in parentheses indicate the estimated height of the local terrain above sea level.

craft, and the storm draft and temperature structure during a typical penetration of an active thunderstorm at 9 km altitude. Traces on the left of the figure represent the complete penetration path; those on the right are an expanded depiction of the electrical structure bracketing the time of an aircraft lightning strike. Aircraft potential with respect to the environment at several wingspan distances is seen to be as large as 400 kV. The vertical electrostatic field change associated with this strike was in excess of 200 kV/m. The general magnitude of the vertical field at 9 km in this large Florida storm is similar to that shown in the 4 to 6 km range in the smaller Colorado storms (Figure 20-38).

Electric fields extend a considerable distance into the clear air surrounding the storm. The finite electrical conductivity of air due to small ion pair production by the cosmic radiation permits a weak current flow of ions to the cloud boundary in response to the storm-generated field. Effects of the development of boundary layer sheaths of space charge of opposite polarity to the main storm charges due to this current flow may complicate the interpretation of measurements of field and field changes taken external to the storm. Theoretical analyses of these problems are given, for example, by Brown et al. [1971], Hoppel and Phillips [1971], Illingsworth [1971], and Klett

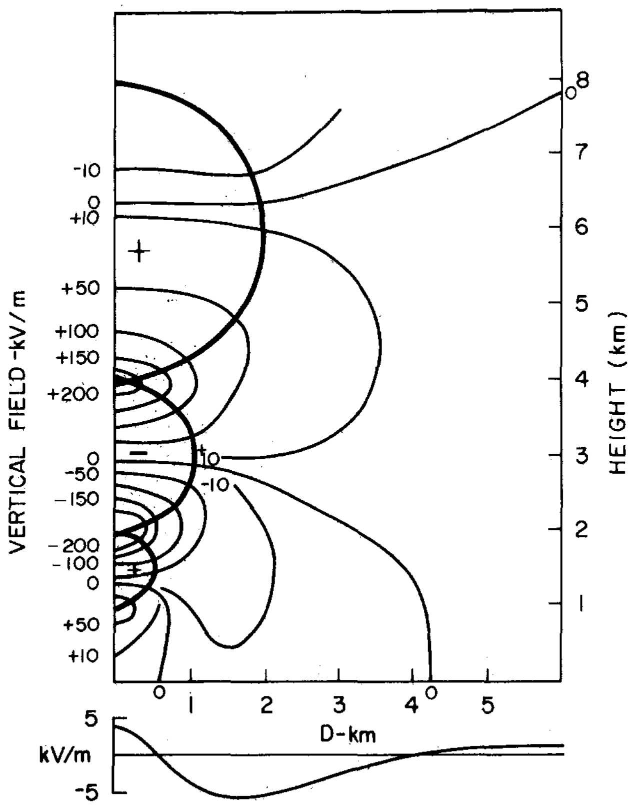

Figure 20-37. Electric field structure of representative European thunderstorms [Simpson and Robinson, 1941].

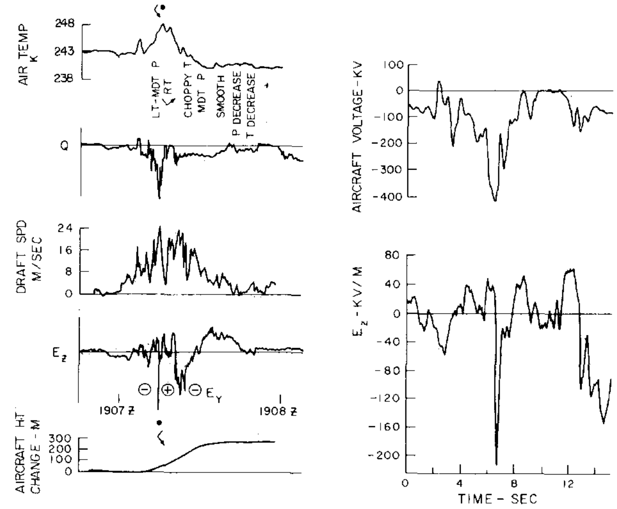

Figure 20-39. Electrical, thermal, and draft structure associated with aircraft lightning strike at 9 km altitude.

[1972]. These studies indicate external measurements, due to a field screening effect by the boundary sheath, may yield underestimates of the major cloud charges and of the true charge center regeneration rates that follow a lightning event. The electrical structure of real storm boundaries is further complicated by the mechanically forced motions of the cloud particles to which the moving small ions attach. These motions are due to the combined horizontal wind and vertical up and down draft velocities associated with the turbulent cloud motions. Given these possible complications in the interpretation of the data, two examples of the field measured in the clear air at high altitudes by instrumented aircraft are shown in Figures 20-40 and 20-41. The first indicates how three components of the electric field incident on an aircraft vary during a track along the western edge of a large Florida storm. The aircraft radar was used to map several contours of storm reflectivity of the storm's precipitation horizontal cross section structure in the vicinity of 9 km altitude. The three field components, E_x oriented along the flight track, E_y directed along the wing, and E_z the vertical component, undergo systematic amplitude

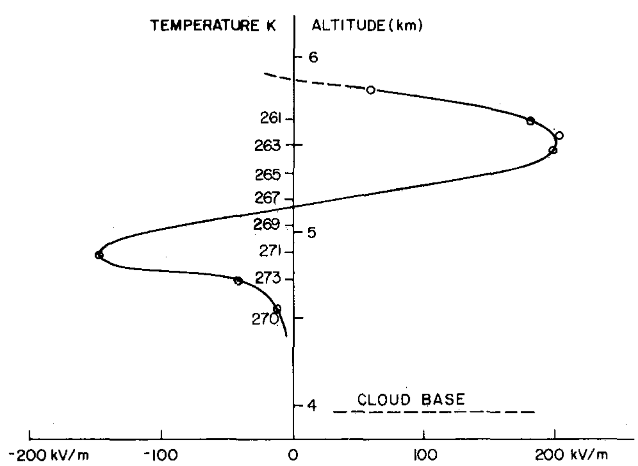

Figure 20-38. Vertical field pattern in Colorado thunderstorms [Parker and Kasemir, 1982].(Reprinted with permission from *IEEE*, © 1982.)

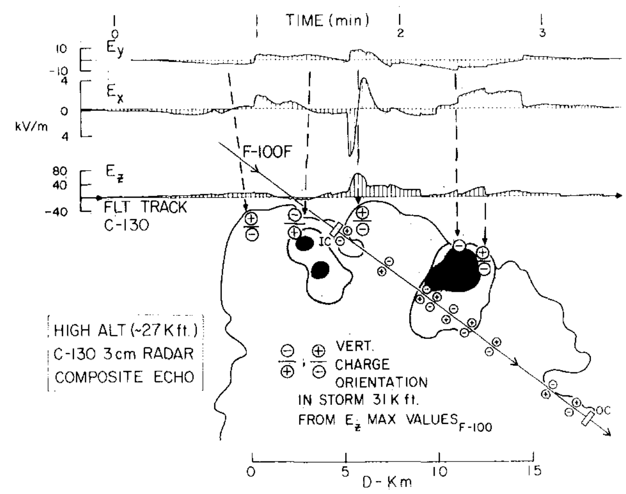

Figure 20-40. Clear air electric field components and radar cross section of a Florida thunderstorm.

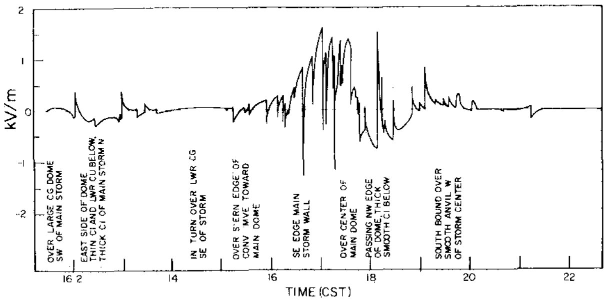

Figure 20-41. Vertical field at 20 km altitude on overflight of an Oklahoma thunderstorm [Fitzgerald and Cunningham, 1965].

variations as the aircraft moves past the major charge concentrations. In general, maxima in E_y and E_z occur when the aircraft is at the closest radial distance to charge centers. The two maxima in E_x are related to boundaries of charge volumes and the zero crossover in E_x occurs near the maxima in E_y and E_z, again indicating the direction to a centroid of the charge center. The charge centers are usually located in the vicinity of the higher values of radar reflectivity but no exact coincidence is found. Field components at midstorm heights may have values to about 50 kV/m in the vicinity of the cloud. Figure 20-41 shows a complex field pattern associated with a U-2 overflight of an Oklahoma thunderstorm. The cloud tops were near 13 km altitude; the aircraft was at 20 km. Field values 7 km above the storm were in the range of 1 kV/m. The sharp discontinuities in the trace are due to the very active lightning activity that was in progress. Other overflight data indicate fields about 3 km above the storm are about 5 kV/m with lightning field changes ranging to 10 kV/m. These fields produce a significant current flow. Gish and Wait [1950] in the first overflight electrical measurements reported the average upward directed current flowing through the upper regions of storms to be about one ampere. The range of currents for a data base of 65 traverses was from 0.1 A to 6 A.

20.2.2 Lightning Characteristics

20.2.2.1 General Phenomenology of the Discharge. The lightning discharge is a complex propagating gas breakdown process. It is thought to originate when a locally strong electric field has developed in the vicinity of small volumes of intense space charge. These differential charge concentrations are trapped on cloud and precipitation particles in the thunderstorm. In midlatitudes lightning usually begins after storm tops have risen to 7 to 9 km and when a radar echo has been present for 10 to 20 minutes. Vertical drafts are normally in the range of 10 to 20 m/s by this time. In high latitudes or winter storm conditions, lightning may occur with cloud tops in the 3 to 4 km range.

Characteristics of the discharge channel are deduced from high-speed photography, optical spectra, and measurement of the acoustic and electromagnetic signals associated with the flash. Further understanding of the physical properties of lightning channels has been greatly advanced through measurements on sparks of several meter lengths as produced by very high voltage generators. Cloud ground strike characteristics have been analyzed from numerous measurements taken at instrumented towers. Test aircraft are in use to study properties of intracloud strokes and their electrical interactions with the aircraft.

The terminology which has evolved to aid in description of the very complex gas electrical breakdown phenomena is rather specialized. The definitions of terms given here is adapted from extensive descriptions of lightning characteristics by Schonland [1956], Uman [1984], and Uman and Krider [1982]. The overall cloud to ground lightning event is defined as a flash. It normally has a duration in the range of 0.1 to 1 s. A frequent value is 0.5 s. A majority of these events neutralize 10s of coulombs of negative charge. However, a significant number of long duration high energy flashes neutralize a positive cloud charge. The common negative flashes frequently are made up of three or four discharge components of about 1 ms duration which are separated in time by 40 to greater than 100 ms. These events are defined as the individual strokes. The time sequence of events starts as a preliminary breakdown process, which may begin in the vicinity of the lower positive and negative charge regions in the cloud as shown in Figures 20-34 and 20-37. The channel extension below cloud base for the first stroke in a flash is called a stepped leader based on the appearance of the chain of bursts of luminosity accompanying the channel motion toward the earth. The initial leader breaks down the dielectric strength of air through a sequence of luminous connecting links of about 50 m lengths. Each segment is formed in about 1 μs, with an average 50 μs delay before formation of the next segment. The return stroke begins when this leader approaches the ground and contacts an upward directed discharge from the ground. This discharge is initiated by the very large potential difference of about 10^8 V between the tip of the approaching leader and the earth's surface. A very rapid equalization of charge in the channel then occurs at a speed of about one third the velocity of light. The most spectacular lightning events such as intense luminosity, high peak current and rate of change of current, rapid electric and magnetic field changes, and production of thunder due to strong heating and expansion of the lightning channel are associated with the return stroke. Subsequent strokes usually follow the existing partially ionized channel. Recharging of this channel from new regions of cloud charge is accomplished by a fast continuous process known as the dart leader. Subsequent return strokes usually do not display the branching structure of the first stroke. The time sequence of events for a three-stroke lightning flash as it would be photographed with a moving film and a stationary camera is summarized in Figure 20-42 adapted from Uman [1984].

Intervals between strokes are variable. A representative

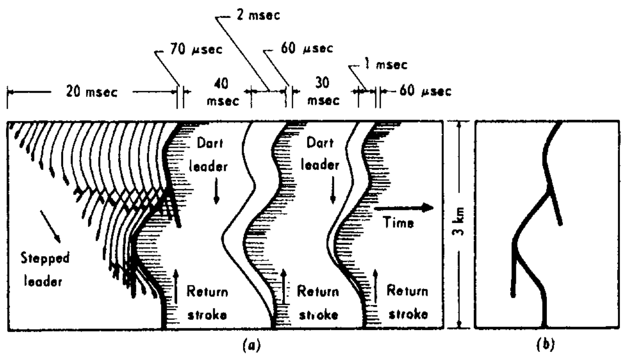

Figure 20-42. Luminous features of cloud ground lightning flash: (a) moving film camera and (b) stationary film camera [Uman, 1984].

value is 50 ms. These are usually preceded by an impulsive dart leader utilizing the existing ionized air to recharge the channel at about a 10^6 m/s rate. The overall strike sequence may involve a time period ranging up to about one second. During the time intervals between the leader-return stroke sequences, the channel can remain weakly conducting for about 100 ms thus permitting a long duration current of the order of 100 A to flow. Most of the actual charge transfer is accomplished by this current. The large peak currents and fast rise time events are associated with the initial portion of the return stroke. Rise times of 0.1 to 2 μs are common. Peak currents may exceed 100 kA although 20 to 30 kA are typical. The statistical distribution of lightning parameters is given in Table 20-8 as prepared by Cianos and Pierce [1972].

20.2.2.2 Characteristics of Radio Frequency Signals due to Lightning. The return stroke current surge generates the most energetic natural radio signals found on earth. The spectral energy has a maximum in the 4 to 8 khz portion of the very low frequency (VLF) band. The stepped leader pulses and a somewhat similar in-cloud channel propagation mode involving current surges known as "K" changes also radiate at VLF with spectral amplitudes about 10% that of return strokes. Long duration strokes also produce extremely low frequency (ELF) signals in the 30 hz to 3 khz band. These VLF and ELF signals can easily be received at distances of many thousand kilometers since they propagate as a guided wave within the spherical shell formed by the earths surface and the lower ionosphere. Very extensive studies of ionospheric properties, radio wave propagation, and long distance direction finding for locating zones of disturbed weather have been conducted using lightning as the signal source. A comprehensive treatment of ELF and VLF propagation and detailed models of natural radio noise sources can be found in Galejs [1972].

The general nature of the radiation produced by a lightning return stroke at a range of some 40 to 100 km from a surface observation point is calculated as a solution to the electromagnetic problem of a current monopole above a flat conducting plane or of the equivalent free-space dipole.

The vertical electric field for this model is given by

$$E_z(t) = \frac{1}{4\pi\varepsilon_0}\left(\frac{M}{d^3} + \frac{1}{cd^2} \times \frac{dM}{dt} + \frac{1}{c^2 d} \times \frac{d^2M}{dt^2}\right) \tag{20.28}$$

Here $M = 2\Sigma qh$ at retarded time $(t - d/c)$ is the charge distribution involved in the flash where q is the charge and h its height, c is the velocity of light, d is the range in meters, and ε_0 is the permittivity of free space. The terms in the equation are generally known as the "electrostatic," "induction," and "radiation" components of the field change.

Table 20-8. Statistical distributions for lightning parameters [Ciamos and Pierce, 1972].

	Percentage of Occurrence				
Parameter[1]	2%	10%	50%	90%	98%
Number of return strokes	10 to 11	5 to 6	2 to 3	—	—
Duration of flash, ms	850	480	180	68	36
Time between strokes, ms	320	170	60	20	11
Return strokes current,[2] kA	140	65	20	6.2	3.1
Charge transfer per flash, C	200	75	15	2.7	1
Time to peak current, μs	12	5.8	1.8	0.66	0.25
Rates of current rise, kA/μs	100	58	22	9.5	5.5
Current half-value time, μs	170	100	45	17	10.5
Duration of continuing current, ms	400	260	160	84	58
Continuing current, A	520	310	140	60	33
Charge of continuing current, C	110	64	26	12	7

[1]Note that all of the parameters are independent. Some judgment must be made in using the values for consistency.
[2]Values for first stroke.

The relative importance of the terms varies as a function of frequency. The radiation term starts to predominate at range $d = c/2\pi f$.

The associated magnetic field is

$$B_\phi(t) = \frac{\mu_0}{4\pi}\left(\frac{1}{d^2} \times \frac{dM}{dt} + \frac{1}{cd} \times \frac{d^2M}{dt^2}\right). \quad (20.29)$$

The terms are known as the "induction" and "radiation" components for this equation. McLain and Uman [1971] have derived exact equations based on more realistic current variations of the "M" term. At ranges beyond 50 km, Equations (20.28) and (20.29) were shown to be accurate. At distances where the channel length is comparable to the range, the assumptions for derivation of the above equations are invalid. Wait [1959] has shown that the $d \ll \ell$, the vertical field is approximately

$$E_z \simeq \frac{2\mu_o f I}{\pi} \times \ln\left(\frac{2\pi d}{\lambda}\right) \quad (20.30)$$

with a corresponding magnetic field

$$B_\phi = \mu_o I/2\pi d, \quad (20.31)$$

where f is the frequency, λ the wavelength, and I the channel current.

A variety of more complex models of the lightning radiation source current shape and of propagation velocity in the channel have been developed to permit more realistic calculations of the electromagnetic field waveforms. Details of the recent status of this work can be found in Lin et al. [1980] and Master et al. [1981].

The VLF-LF electric field spectra associated with Florida thunderstorms has recently been obtained for source distances ranging from 1.5 km to 200 km. Table 20-9 taken

Table 20-9. Mean and standard deviations (s.d.) of electric field spectra in decibels for various distances [Serhan et al., 1980].

		First strokes			Subsequent strokes		
Frequency kHz	Distance, km	Number of strokes	Mean, dB	s.d., dB	Number of strokes	Mean, dB	s.d., dB
2	1.5	6	−15.8	4.0			
5	1.5	6	−19.2	3.0			
10	1.5	6	−24.2	3.2			
100	1.5	6	−43.6	3.4			
300	1.5	6	−52.0	3.4			
2	4.0	4	−35.0	2.4	4	−39.8	2.8
5	4.0	4	−38.8	2.2	4	−41.6	2.8
10	4.0	4	−44.2	2.6	4	−47.0	2.0
100	4.0	4	−64.0	1.8	4	−67.2	3.2
300	4.0	4	−71.2	3.4	4	−72.0	2.2
2	7.0	9	−44.6	3.2	8	−50.0	2.0
5	7.0	9	−46.8	1.8	8	−51.0	2.2
10	7.0	9	−53.4	2.2	8	−56.6	3.2
100	7.0	9	−72.8	4.0	8	−72.8	4.2
300	7.0	9	−77.0	3.2	8	−82.2	4.0
2	10.0	6	−51.4	3.8	15	−56.0	4.8
5	10.0	6	−53.4	3.2	15	−57.5	4.2
10	10.0	6	−58.8	3.6	15	−64.6	4.0
100	10.0	6	−75.2	6.0	15	−80.2	7.0
300	10.0	6	−81.4	2.6	15	−85.6	3.4
2	50.0	13	−71.4	6.4	21	−77.0	4.5
5	50.0	13	−69.2	6.4	21	−75.2	4.5
10	50.0	13	−76.2	4.6	21	−79.4	3.0
100	50.0	13	−92.0	6.6	21	−95.0	4.0
300	50.0	13	−103.6	6.6	21	−108.6	4.8
2	200.0	22	−86.0	5.6	34	−89.3	5.0
5	200.0	22	−83.6	5.1	34	−87.0	3.6
10	200.0	22	−88.2	4.1	34	−91.2	3.6
100	200.0	22	−105.6	5.4	34	−108.0	4.0
300	200.0	22	−124.5	6.1	34	−127.0	6.2

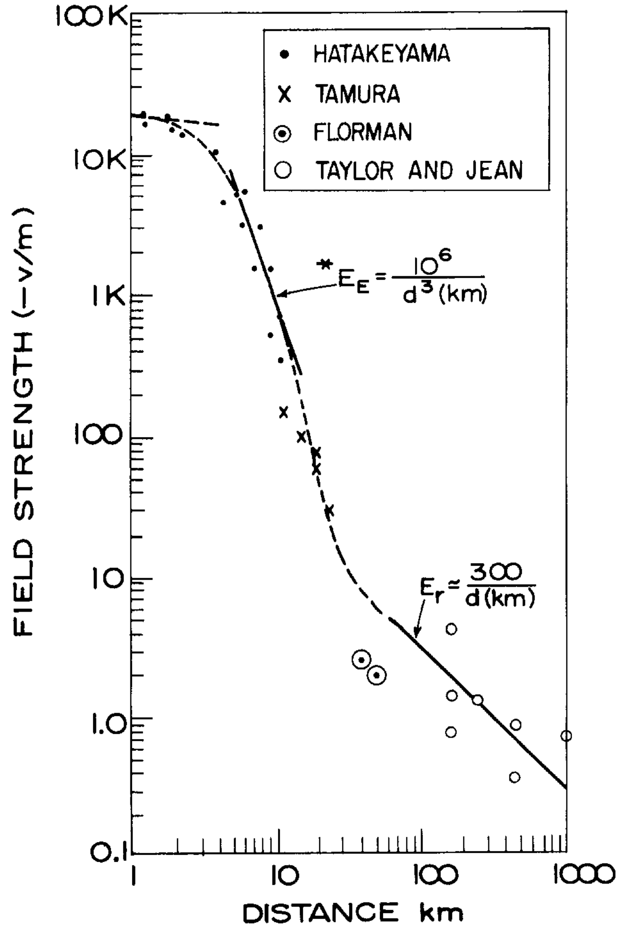

Figure 20-43. Peak electric field variation vs distance from lightning discharges [Watt, 1969].

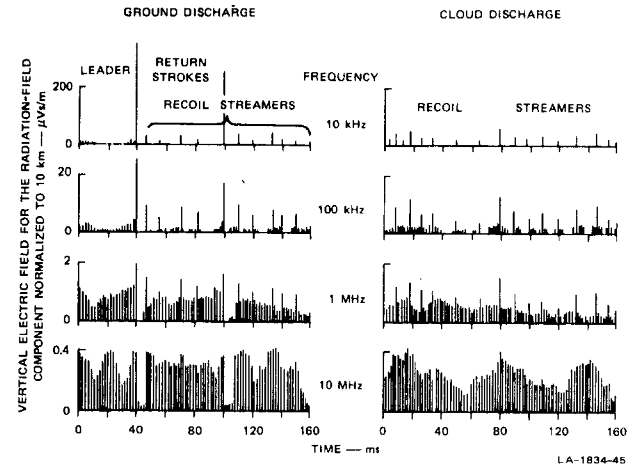

Figure 20-45. The structure of the fields radiated by lightning as a function of time and frequency [Cianos and Pierce, 1972].

from Serhan et al. [1980] gives the db values as 20 times the magnitude (Vs/m) of the frequency spectrum for frequencies ranging from 2 khz to 300 khz.

Earlier data on the peak electric field vs source distance as summarized by Watt [1969] is given in Figure 20-43. The transitions of slope from a nearly constant field associated with a nearby flash to the $1/d^3$ electrostatic field regime and final 1/d radiation field are clearly depicted. The peak signal amplitude in a 1 khz bandwidth as a function of received signal frequency is given in Figure 20-44. Data of the investigators listed in the figures have been normalized

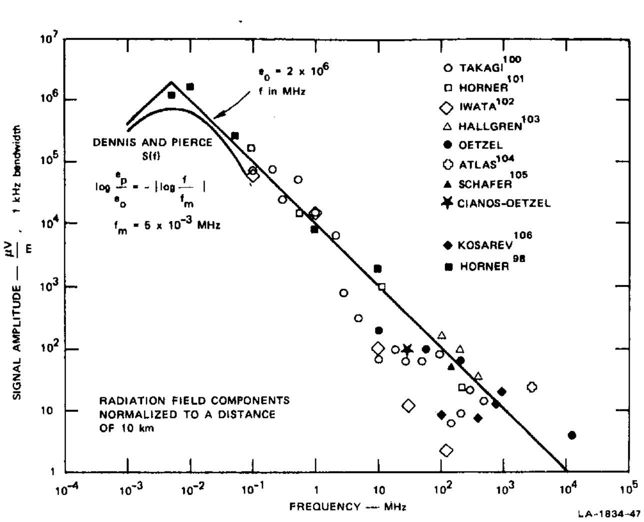

Figure 20-44. Peak received amplitude as a function of frequency [Cianos and Pierce, 1972].

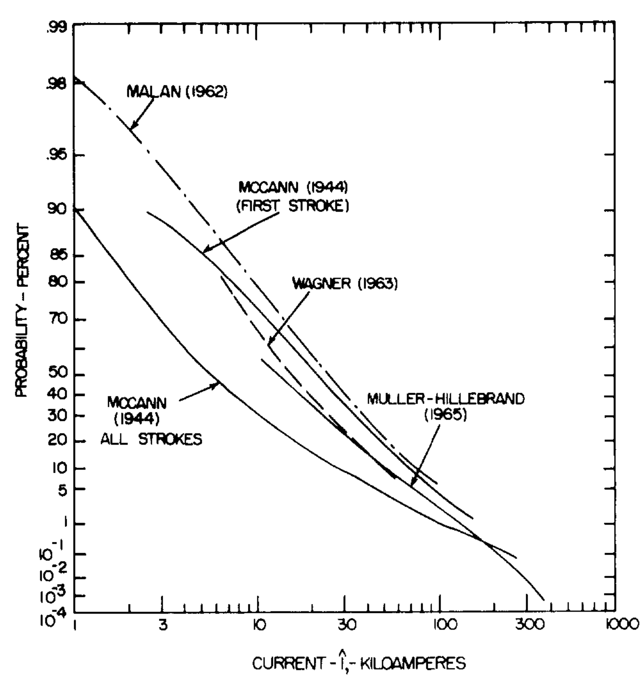

Figure 20-46. Probability distribution of current peaks in a lightning flash [Galejs, 1972].

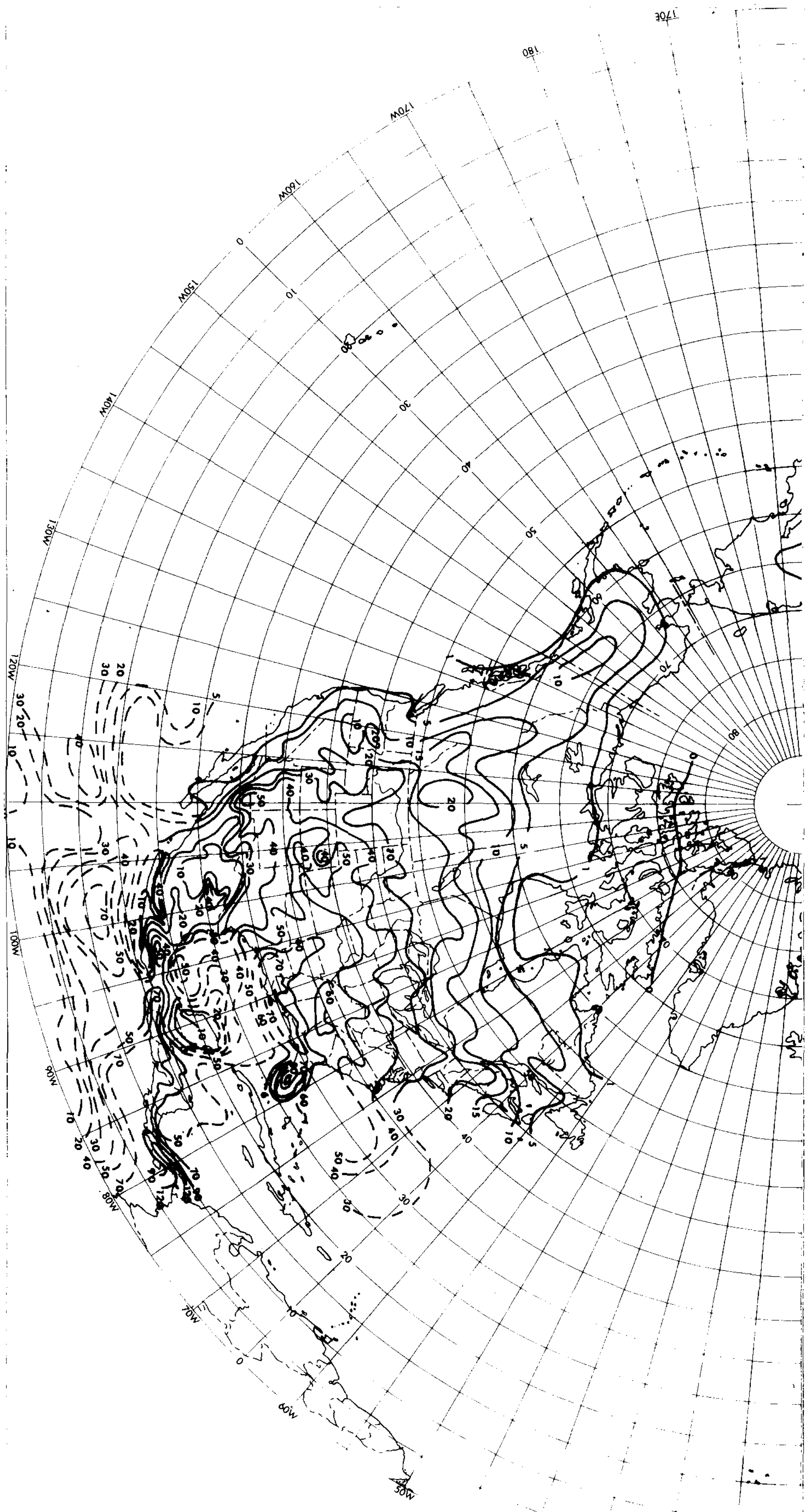

Figure 20-47. Annual distribution of thunderstorm days for North America.

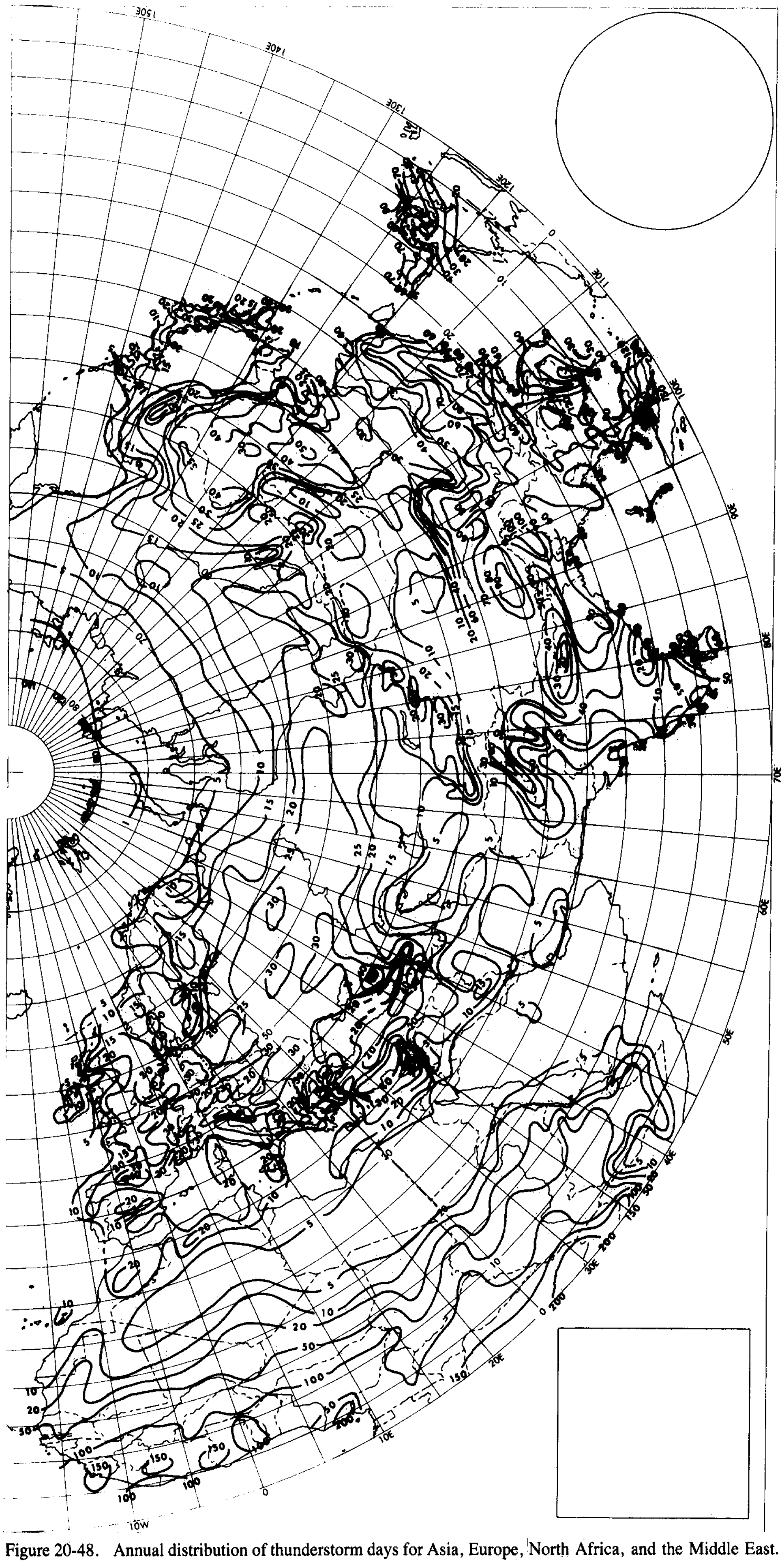

Figure 20-48. Annual distribution of thunderstorm days for Asia, Europe, North Africa, and the Middle East.

to a source distance of 10 km and presented by Cianos and Pierce [1972].

The amplitude variation patterns of the radio noise burst due to a lightning event are complex and have a considerable variation of structure at different frequencies. Figure 20-45, also due to Cianos and Pierce [1972] depicts the general nature of the received fields due to cloud-ground and intra-cloud flashes at four frequencies. The terminology "recoil streamers" refers to within cloud current surges associated with the channel contacting small highly charged regions. These are the same as the "K" changes previously described.

The magnitude of the various parameters of lightning phenomena vary over a wide range. It is common to assume that the logarithm of the parameter of interest can be fit to the normal or Gaussian statistical distribution. For example the probability that a peak current I exceeds a reference current I_o can be written as

$$P(I > I_o) = \frac{1}{\sigma\sqrt{2\pi}} \int_{I_o}^{\infty} \frac{dI}{I} \exp\left[\frac{-(\ln I - m)^2}{2\sigma^2}\right]$$

$$= \frac{1}{2}\left[1 - \operatorname{erf}\left(\frac{\ln I_o - m}{\sigma\sqrt{2}}\right)\right],$$

where m is the median value of ln I and σ is the standard deviation. Galejs [1972] has summarized data on peak currents involved in power transmission line flashes as measured in several countries. The probability distribution is shown in Figure 20-46.

In recent years the relation of VHF radio noise to channel characteristics has become much better known as a result of studies of incipient lightning streamers and subsequent channel development. As suggested by Figure 20-45, the noise structure is very complex, but it appears as indicated by Proctor [1981] that irregular patterns of short individual pulses and of longer bursts of pulses occur at VHF. Pulse rates range from 10^3 to greater than 10^5/s with individual pulse durations from about 0.1 to 1 μs. The stronger pulses are thought to be associated with ionization produced at the tip of the channel extension into previously neutral air while weaker noise bursts are associated with reintensification of ionization in a decaying channel due to dart leader or recoil streamer reconnections with the main charge sources. Streamer propagation velocities range from 10^4 to 10^7 m/s with current in the channel of the order of 100 A. A charge density of around 10^{-3} C/m of channel length is established in the process.

Kachurin et al. [1974] demonstrated systematic changes in the RF spectra over a range 0.1 to 300 Mhz as convective clouds developed to the thunderstorm stage. Short bursts of noise, usually of 10 to 15 ms duration, occurred for 5 to 10 min preceding lightning activity. At 100 Khz, the burst amplitudes were about 100 μV/m in 1 Khz bandwidth as normalized to 10 km distance. With storm development, a secondary maximum in the pulse duration statistics was found to occur in the 100 to 150 ms interval. Concurrently the 100 Khz signal amplitude increased to about 50 000 μV/m Khz normalized as above.

20.2.3 Precipitation Static Characteristics

Flight through various haze conditions, dust or sand storms, rain, and particularly through snow and ice crystal clouds, causes a considerable accumulation of charge and an aircraft voltage of the order of 100 kV with respect to the environment. Charge accumulation results from collisions of the cloud and precipitation particles with the aircraft. The magnitude of the charging current is related to the mean net charge transferred per impact and the number of particles intercepted per unit time. Thus it is proportional to the frontal area of the aircraft. Discharge takes place through the engine exhaust and by corona from the high curvature portions of the airframe. The corona pulses have a serious effect on radio reception below about 30 Mhz and at times interfere with VHF and UHF reception. An early discussion of this phenomenon and of the development of corona-resistant antenna sheaths and low noise dischargers is given in a series of articles by Gunn et al. [1946]. Development of later dischargers for jet aircraft is described by Nanevicz and Tanner [1964].

High-speed aircraft have additional noise problems. At speeds above 130 m/s the noise level may increase at rates up to the sixth power of the speed [Couch, 1960]. Three noise generating mechanisms are corona pulses, an effect called streamering (flashover to the airframe of charge built up on dielectric surfaces), and an effect due to antenna pickup of sudden changes in particle-impact voltage. The latter noise is at least 54 dB below the streamering noise level. The spectrum of impact noise decreases inversely with frequency. The streamering spectrum is nearly flat to 160 Khz, rolling off to 3 dB down at 480 Khz. Corona pulses have rise times of a few nanoseconds with decay to 50% in 30 ns at sea level pressure. At 10 km altitude the rise and decay times shift to 20 and 100 ns with the reduced pressure. Wide band RF noise is easily generated by these pulses. It must be decoupled from the aircraft antennas. This is accomplished through use of very sharply pointed static discharge points which act to reduce the amplitude of the corona pulses and by the use of high resistance rods extending from trailing outboard locations on aircraft. These rods provide a mechanical connection for the points and maintain them at the same DC potential as the aircraft. The resistance and distributed capacitance of the installation act as a filter to greatly reduce the radio frequency content of the discharge current.

20.2.4 Distribution and Duration of Thunderstorms

About 50 000 thunderstorms occur every day throughout the world and, on the average, about 2000 storms are in progress at any time. Large scale charts of the frequency of occurrence of storms over the earth as a function of location and month were published by the World Meteorological Organization, Geneva, Switzerland and were reprinted in the 1960 edition of the Handbook of Geophysics. A thunderstorm day is internationally defined as a day on which thunder is heard. No account is taken of the duration or number of storms on a given day in the tabulation of these statistics. As illustrations of the data available, new more detailed charts have been prepared taking into account airfield data compiled by the USAF Environmental Technical Applications Center (ETAC), some topographic features, and the probable distribution across national boundaries. These are shown as Figures 20-47 and 20-48. Data from Stekol'nikov [1955] and from Arkhipova [1957] have been used for assistance in constructing the maps for the USSR. The accuracy of charts such as these could be considerably improved through addition of satellite and RF direction finder information. In general about one half the storms last for one hour, a quarter for two hours. Complex systems may produce activity for many hours. A comprehensive discussion and monthly summaries of thunderstorm days at a number of stations in the USSR can be found in Arkhipova [1957].

REFERENCES

Anderson, F.J. and G.D. Freier, "Interactions of the Thunderstorms with a Conducting Atmosphere," *J. Geophys. Res.*, **74:** 5390, 1969.

Arkhipova, E.P., "Maps of the Geographic Distribution of the Number of Thunderstorm Days in the USSR" (Karty Geograficheskogo Raspredeleniia Chisla Dnei s Grozoi na Territorii SSSR), *Leningrad. Glavnaia Geofizicheskaia Observatoria, Trudy,* **74:** 41–60 1957 (Engl. transl. USWB), 1960.

Aspinall, W.P., "Mechanical Transfer Currents of Atmospheric Electricity," *J. Geophys. Res.*, **77:** 3196, 1972.

Bauer, L.A., "Sunspots and Annual Variations of Atmospheric Electricity with Special Reference to Carnegie Observations 1915–1921," *Res. Dep. Terr. Magn. Carnegie Inst. Wash.*, **175**(5): 359, 1926.

Berger, K., "Novel Observations on Lightning Discharges, Results of Research on Mount San Salvatore," *J. Franklin Inst.*, **283:** 478, 1967.

Bossolasco, M., I. Dagnino, A. Elena, and G. Flocchini, "Solar Flare Control of Thunderstorm Activity," in *Studi in onore di G. Aliverti,* Instituto Universitario Navale Di Napoli, 213, 1972.

Braham, Jr., R.R., "The Water and Energy Budgets of the Thunderstorm and Their Relation to Thunderstorm Development," *J. Meteor.*, **9:** 227, 1952.

Bricard, P.J., "L'equilibre Ionique de la Basse Atmosphere," *J. Geophys. Res.*, **54:** 39, 1949.

Brown, K.A., P.R. Krehbiel, C.B. Moore, and G.N. Sargent, "Electrical Screening Layers Around Charged Clouds," *J. Geophys. Res.*, **76:** 2825, 1971.

Bruce, C.E.R. and R.H. Golde, "The Lightning Discharge," *J. Inst. Elect. Engrs. London*, **88:** 487, 1941.

Burke, H.K. and A.A. Few, "Direct Measurement of the Atmospheric Conduction Current," *J. Geophys. Res.*, **83:** 3093, 1978.

Byers, H.R. and R.R. Braham, *The Thunderstorm,* U.S. Government Printing Office, Washington, D.C., 1949.

Chalmers, J.A., *Atmospheric Electricity, 2nd Edition,* Pergamon Press, New York, 1967.

Chapman, S., "Corona-Point-Discharge in Wind and Application to Thunderclouds," in *Recent Advances in Atmospheric Electricity,* edited by L.G. Smith, Pergamon Press, New York, 1958.

Christian, H., C.R. Holmes, J.W. Bullock, W. Gaskell, A.J. Illingworth, and J. Latham, "Airborne and Ground-Based Studies of Thunderstorms in the Vicinity of Langmuir Laboratory," *Quart. J. Roy. Meteor. Soc.*, **106:** 159, 1980.

Cianos, N. and E.T. Pierce, "A Ground-Lightning Environment for Engineering Usage," Stanford Research Institute, Report 1, Contract LJS-2817-A3, SRI Project 1834, 1972.

Clarence, N.D. and D.J. Malan, "Preliminary Discharge Processes in Lightning Flashes to Ground," *Quart. J. Roy. Meteorol. Soc.*, **83:** 161, 1957.

Clifford, D.W. "Another Look at Aircraft-Triggered Lightning," FAA/NASA/FIT Symposium on Lightning Technology, Hampton, Va., 1980.

Cobb, W.E., "Evidence of Solar Influence on the Atmospheric Electric Elements at Mauna Loa Observatory," *Monthly Weather Rev.*, **95:** 12, 1967.

Cole, R.K. and E.T. Pierce, "Electrification in the Earth's Atmosphere for Altitudes between 0 and 100 km," *J. Geophys. Res.*, **70:** 2735, 1965.

Couch, P.W., "Precipitation Static on Modern Aircraft," in *Electromagnetic Wave Propagation,* edited by M. Desirant and J.L. Michiels, Academic Press, New York, 1960.

Crozier, W.D., "Atmospheric Electrical Profiles below Three Meters," *J. Geophys. Res.*, **70:** 2785, 1965.

Dennis, A.S., and E.T. Pierce, "The Return Stroke of the Lightning Flash to Earth as a Source of VLF Atmospherics," *Radio Sci.*, **68D:** 777, 1964.

DuBro, G.A. (ed.), *Atmospheric Electricity-Aircraft Interaction,* AGARD Lecture Series 110, Technical Editing and Reproduction Ltd., London (Avail. NTIS), 1980.

Ferguson, E.E., [including all references therein], "Ion Chemistry of the Middle Atmosphere," in *NASA CP-2090,* National Aeronautics and Space Administration, p. 71–88, 1979.

Fischer, H.J. and R. Muhleisen, "Variationen des Ionospharen-potentials und der Weltgewittertatigkeit im elfjahrigen solaren Zyklus," *Meteorologische Rundschau,* **25:**6., 1972.

Fisher, F.A. and J.A. Plumer, *Lightning Protection of Aircraft,* NASA Reference Publication 1008, U.S. Government Printing Office, Washington, D.C., 1977.

Fitzgerald, D.R., "Theoretical and Experimental Studies of Convective Cloud Electrification," Final Report, Contract AF 19(604)-1552, AD 98761, 1956.

Fitzgerald, D.R., "Some Theoretical Aspects of the Relation of Surface Electric Field Observations to Cloud Charge Distributions," *J. Meteor.*, **14:** 505, 1957.

Fitzgerald, D.R., "Probable Aircraft Triggering of Lightning in Certain Thunderstorms," *Monthly Weather Rev.*, **95:** 835, 1967.

Fitzgerald, D.R. and H.R. Byers, "Aircraft Observations of Convective Cloud Electrification," in *Recent Advances in Atmospheric Electricity,* edited by L.G. Smith, Pergamon Press, New York, 1958.

Fitzgerald, D.R. and R.M. Cunningham, "Multiple Aircraft Studies of the Electrical Properties of Thunderstorms," *Proceedings International Conference on Cloud Physics,* Tokyo and Sapporo, Japan, 24 May–1 June, p. 157, 1965.

Flohn, H. "Solare Korpuskularausbruche und Gewitterfrequenz, (Solar Corpuscular Eruptions and Thunderstorm Frequency)", in *Das Gewitter*, edited by H. Israel, Akad. Verlag Gesel., Leipzig, 143, 1950.

Forbush, S.E., "World-wide Cosmic Ray Variations, 1937–1952," *J. Geophys. Res.*, **59:** 525, 1954.

Fulks, G.J., "Solar Modulation of Galactic Cosmic Ray Electrons, Protons, and Alphas," *J. Geophys. Res.*, **80:** 1701, 1975.

Galejs, J., *Terrestrial Propagation of Long Electromagnetic Waves,* Pergamon Press, New York, 1972.

Gathman, S.C., "The Effects of Local Atmospheric Space Charge on Surface Electric Fields," *Trans. (AGU)* **48:** 107, 1967.

Gish, O.H. and G.R. Wait, "Thunderstorms and the Earth's General Electrification," *J. Geophys. Res.*, **55:** 473, 1950.

Golde, R.H. (ed.), *Lightning*, Vol. 1, Physics of Lightning, Vol. 2, Lightning Protection, Academic Press, New York, 1977.

Gunn, R., "Electric Field Intensity Inside of Natural Clouds," *J. Appl. Phys.*, **19:** 481, 1948.

Gunn, R., W.C. Hall, and G.D. Kinzer, "Army-Navy Precipitation Static Project," *Proc. Inst. Radio Engrs.*, **34** (4&5), 1946.

Harrison, H.T., "UAL Turbojet Experience with Electrical Discharges," *UAL Meteorology Circular No. 57*, United Airlines, Chicago, 1967.

Harrison, L.P., "Lightning Discharges to Aircraft and Associated Meteorological Conditions," NACA Tech. Note 1001, Washington, D.C., 1946.

Hays, P.B. and R.G. Roble, "A Quasi-Static Model of Global Atmospheric Electricity, 1. The Lower Atmosphere," *J. Geophys. Res.*, **84,** 3291, 1979.

Herman, J.R. and R.A. Goldberg, "Sun, Weather and Climate," *NASA SP-426*, National Aeronautics and Space Administration, Washington, D.C, 1978a.

Herman, J.R. and R.A. Goldberg, "Initiation of Non-Tropical Thunderstorms by Solar Activity," *J. Atmos. Terr. Phys.*, **40,** 121, 1978b.

Hogg, A.R., "Air-Earth Observations in Various Localities—Arch. Meteor.," Wien A., 3.40, 1950.

Holmes, C.R., E.W. Szymanski, S.J. Szymanski, and C.B. Moore, "Radar and Acoustic Study of Lightning," *J. Geophys. Res.*, **85:** 7517, 1980.

Holzer, R.E. and D.S. Saxon, "Distribution of Electrical Conduction Currents in the Vicinity of Thunderstorms," *J. Geophys. Res.*, **57:** 207, 1952.

Hoppel, W.A., "Electrode Effect: Comparison of Theory and Measurement," *Proceedings 4th International Conference on the Universal Aspects of Atmospheric Electricity, II*, 167, 1969.

Hoppel, W.A. and B.B. Phillips, "The Electrical Shielding Layer Around Charged Clouds and Its Role in Thunderstorm Electricity," *J. Atmos. Sci.*, **28:** 1258, 1971.

Illingsworth, A.J., "The Variation of the Electric Field after Lightning and the Conductivity within Thunderclouds," *Quart. J. Roy. Met. Soc.*, **97:** 440–456, 1971.

Israël, H. (ed.), *Das Gewitter*, Akad. Verlag Gesel., Leipzig, 1950.

Israël, H., and H. Dolezalek, *Atmospheric Electricity, Vol II*, Israel Program for Scientific Translations, Jerusalem, 1973.

Jacobson, E.A. and E.P. Krider, "Electrostatic Field Changes Produced by Florida Lightning," *J. Atmos. Sci.*, **33:** 103, 1976.

Kachurin, L.G., M.I. Karmov, and Kh.Kh. Medaliyev, "The Principal Characteristics of the Radio Emission of Convective Clouds," Isv., *Atmos. Oceanic Phys.*, **10:** 1163–1169, 1974.

Kent, D.W. and M.A. Pomerantz, "Cosmic Ray Intensity Variations in the Lower Atmosphere," *J. Geophys. Res.*, **76:** 1652, 1971.

Kitagawa, N. and M. Brook, "A Comparison of Intracloud and Cloud-to-Ground Lightning Discharges," *J. Geophys. Res.*, **65:** 1189, 1960.

Klett, J.D., "Charge Screening Layers Around Electrified Clouds," *J. Geophys. Res.*, **77:** 3187, 1972.

Krider, E.P., G.A. Dawson, and M.A. Uman, "The Peak Power and Energy Dissipation in a Single-Stroke Lightning Flash," *J. Geophys. Res.*, **73:** 3335, 1968.

Krider, E.P., R.C. Noggle, and M.A. Uman, "A Gated, Wideband Magnetic Direction Finder for Lightning Return Strokes," *J. Appl. Meteor.*, **15:** 301, 1976.

Lhermitte, R. and P.R. Krehbiel, "Doppler Radar and Radio Observations of Thunderstorms," *IEEE Trans. Geosci. Electron.*, **GE-17:** 162, 1979.

Lin, Y.T., M.A. Uman, and R.B. Standler, "Lightning Return Stroke Models," *J. Geophys. Res.*, **85:** 1571, 1980.

Livingston, J.M. and E.P. Krider, "Electric Fields Produced by Florida Thunderstorms," *J. Geophys. Res.*, **83:** 385, 1978.

Loeb, L.B., "The Mechanisms of Stepped and Dart Leaders in Cloud-to-Ground Lightning Strokes," *J. Geophys. Res.*, **71:** 4711, 1966.

Magono, C., *Thunderstorms*, Elsevier Press, Amsterdam, 1980.

Malan, D.J., *Physics of Lightning*, English Universities Press, London, 1963.

Master, M.J., M.A. Uman, Y.T. Lin, and R.B. Standler, "Calculations of Lightning Return Stroke Electric and Magnetic Fields Above Ground," *J. Geophys. Res.*, **86:** 12, 127, 1981.

Mauchly, S.J., "On the Diurnal Variation of the Potential Gradient of Atmospheric Electricity," *Terr. Mag. Atmos. Elec.*, **28:** 61, 1923.

McLain, D.K. and M.A. Uman, "Exact Expression and Moment Approximation for the Electric Field Intensity of the Lightning Return Stroke," *J. Geophys. Res.*, **76:** 2101, 1971.

Morita, Y., H. Ishikawa, and M. Kanada, "The Vertical Profiles of the Small Ion Density and the Electric Conductivity in the Atmosphere up to 19 km," *J. Geophys. Res.*, **76:** 3431–3436, 1971.

Mozer, F.S. and R. Serlin, "Magnetospheric Electric Field Measurements with Balloons," *J. Geophys. Res.*, **74:** 4739, 1969.

Muhleisen, R., "Electrode Effect Measurements Above the Sea," *J. Atmos. Terr. Phys.*, **20:** 79, 1961.

Muhleisen, R., "Neue Ergebnisse und Probleme" in *der Luftelektrizitat. Zs. Geophysik*, **37:** 759, 1971.

Nanevicz, J.E., and R.L. Tanner, "Some Techniques for the Elimination of Corona Discharge Noise in Aircraft Antennas," *Proc. IEEE*, **52:** 53, 1964.

Ogawa, T. and M. Brook, "Charge Distribution in Thunderstorm Clouds," *Quart. J. Roy. Meteor. Soc.*, **95:** 513, 1969.

Paltridge, G.W., "Experimental Measurements of the Small Ion Density and Electrical Conductivity of the Stratosphere," *J. Geophys. Res.*, **70:** 2751, 1965.

Park, C.G. and M. Dejnakarintra, "Penetration of Thundercloud Electric Fields into the Ionosphere and Magnetosphere, 1. Middle and Subauroral Latitudes," *J. Geophys. Res.*, **78:** 6623, 1973.

Parker, L.W., and H.W. Kasemir, "Airborne Warning Systems for Natural and Aircraft-Initiated Lightning," *IEEE Trans. Electr. Compatib.*, **EMC-24:** 137, 1982.

Pierce, E.T., "Electrostatic Field-Changes Due to Lightning Discharges," *Quart. J. Roy. Meteor. Soc.*, p. 211, 1955.

Proctor, D.E., "VHF Radio Pictures of Cloud Flashes," *J. Geophys. Res.*, **86:** 4041, 1981.

Reid, G.C. [including all references therein], "The Middle Atmosphere," in *NASA CP-2090*, National Aeronautics and Space Administration, 27–42, 1979.

Reiter, R., "Solar Flares and Their Impact on Potential Gradient and Air-Earth Current Characteristics at High Mountain Stations," *Pure Appl. Geophys.*, **72:** 259, 1969.

Rosen, J.M., D.J. Hofmann, W. Gringel, J. Berlinski, S. Michnowski, Y. Morita, T. Ogawa, and D. Olson, *Results of an International Workshop on Atmospheric Electrical Measurements*, Dept. of Physics and Astronomy, University of Wyoming, Laramie, 1980.

Rosen, J.M. and D.J. Hoffman, "Balloon-Borne Measurements of the Small Ion Concentration," *J. Geophys Res.*, **86:** 7399, 1981a.

Rosen, J.M. and D.J. Hoffman, "Balloon-Borne Measurements of Electrical Conductivity, Mobility and the Recombination Coefficient," *J. Geophys. Res.*, **86:** 7406, 1981b.

Rust, W.D. and C.B. Moore, "Electrical Conditions Near the Bases of Thunderclouds Over New Mexico," *Quart. J. Roy. Met. Soc.*, **100:** 450, 1974.

Rustan, P.L., M.A. Uman, D.G. Childers, and W.H. Beasley, "Lightning Source Locations from VHF Radiation Data for a Flash at Kennedy Space Center," *J. Geophys. Res.*, **85:** 4893, 1980.

Sagalyn, R.C. and D.R. Fitzgerald, "Atmospheric Electricity," in *Handbook of Geophysics and Space Environments*, Office of Aerospace Research, U.S. Air Force, 1965.

Sagalyn, R.C. and G.A. Faucher, "Aircraft Investigation of the Large Ion Content and Conductivity of the Atmosphere and Their Relation to Meteorological Factors," *J. Atmos. Terr. Phys.*, **5:**253, 1954.

Sagalyn, R.C. and G.A. Faucher, "Space and Time Variations of Nuclei and Electrical Conductivity of the Atmosphere," *Quart. J. Roy. Meteorol. Soc.*, **82:**428, 1956.

Schonland, B.F.J., "The Lightning Discharge," *Handbuch der Physik*, **22:** 576–628, Springer Verlag OH , Berlin, 1956.

Schonland, B.F.J., *The Flight of Thunderbolts*, 2nd ed., Clarendon Press, Oxford, U.K., 1964.

Serhan, G.I., M.A. Uman, D.G. Childers, and Y.T. Lin, "The RF Spectra of First and Subsequent Lightning Return Strokes in the 1- to 200-km Range," *Radio Sci.*, **15:** 1089, 1980.

Simpson, G.D., and G.D. Robinson, "The Distribution of Electricity in Thunderclouds, II," *Proc. Roy. Soc.*, **A 177:** 281, 1941.

Smith, L.G. (ed.), *Recent Advances in Atmospheric Electricity*, Pergamon Press, New York, 1958.

Stekol'nikov, I.S., *Study of Lightning and Lightning Protection*, **JPRS 29:** 407, trans. of *Izucheniye Molnii i Grozozashchita*, Moscow, 1955.

Stergis, C.G., G.C. Rein, and T. Kangas, "Electric Field Measurements in the Stratosphere" and "Electric Field Measurements above Thunderstorms," *J. Atmos. Terr. Phys.*, **11:** 77–83, 1957.

Takagi, M., Y. Morita, Y. Kondo, and H. Ishikawa, "Balloon Observations of Atmospheric Electrical Elements and Aerosols in the Lower Stratosphere," *Proceedings of VI International Conference on Atmospheric Electricity*, University Manchester Inst. of Science and Technology, England, 1978.

Takagi, M., Y. Morita, Y. Kondo, and H. Ishikawa, "Balloon Observations of Atmospheric Electrical Elements and Aerosols in the Lower Stratosphere," *5th International Conference on Atmospheric Electricity*, Garmisch-Partenkirchen, Germany, 1980.

Takeuti, T., M. Nakano, M. Nagatani, and H. Nakada, "On Lightning Discharges in Winter Thunderstorms," *J. Meteorol. Soc. Japan*, **51:** 494, 1973.

Taylor, W.L., "Radiation Field Characteristics of Lightning Discharges in the Band 1 kc/s to 100 kc/s," *J. Res. Natl. Bur. Stds.*, **67D:** 539, 1963.

Teer, T.L. and A.A. Few, "Horizontal Lightning," *J. Geophys. Res.*, **79:** 3436, 1974.

Tiller, J.A., M.A. Uman, Y.T. Lin, and R.D. Brantley, "Electric Field Statistics for Close Lightning Return Strokes Near Gainesville, Florida," *J. Geophys. Res.*, **81:** 4430, 1976.

Uchikawa, K., "On the Seasonal Variations of the Atmospheric Electric Elements," *Pure Appl. Geophys.*, **100**(8): 54, 1972

Uman, M.A., *Lightning*, Dover, New York, 1984.

Uman, M.A. and E.P. Krider, "A Review of Natural Lightning: Experimental Data and Modeling," *IEEE Trans. on Electromagnetic Capability*, **EMC-24:** 79–112, 1982.

Wait, J.R., *Electromagnetic Radiation from Cylindrical Structures*, Pergamon Press, New York, 1959.

Watt, A.D., *V.L.F. Radio Engineering*, Pergamon Press, New York, 1967.

Watt, A.D., "ELF Electric Fields from Thunderstorms," *J. Res. Natl. Bur. Stds.*, **64D:** 425, 1969.

Webber, W., "The Production of Free Electrons in the Ionospheric D-Layer by Solar and Galactic Cosmic Rays and the Resultant Absorption of Radio Waves," *J. Geophys. Res.*, **67:** 5091, 1962.

Weber, M.E., H.J. Christian, A.A. Few, and M.F. Stewart, "A Thundercloud Electric Field Sounding: Charge Distribution and Lightning," *J. Geophys. Res.*, **87:** 7158, 1982.

Weidman, C.D. and E. P. Krider, "The Radiation Field Waveforms Produced by Intracloud Lightning Discharge Processes," *J. Geophys. Res.*, **84:** 3159: 1979.

Williams, J.C., "Some Properties of the Lower Positive Charge in Thunderclouds," in *Recent Advances in Atmospheric Electricity*, edited by L.G. Smith, Pergamon Press, New York, 1958.

Wilson, C.T.R., "On Some Determinations of the Sign and Magnitude of Electric Discharges in Lightning Flashes," *Proc. Roy. Soc.*, **A 92:** 555, 1916.

Winn, W.P., C.B. Moore, and C.R. Holmes, "Electric Field Structure in an Active Part of a Small, Isolated Thundercloud," *J. Geophys. Res.*, **86:** 1187, 1981.

Winn, W.P., G.W. Schwede, and C.B. Moore, "Measurements of Electric Fields in Thunderclouds," *J. Geophys. Res.*, **79:** 1761, 1974.

World Meteorological Organization, "World Distribution of Thunderstorm Days" Geneva, WMO No. 21, 1956.